

# The Millennium Galaxy Catalogue: the space density and surface brightness distribution(s) of galaxies

S.P. Driver,<sup>1,2\*</sup>† J. Liske,<sup>3</sup> N.J.G. Cross,<sup>4</sup> R. De Propris<sup>1,2</sup> and P.D. Allen<sup>1</sup>

<sup>1</sup>Research School of Astronomy and Astrophysics, Australian National University, Cotter Road, Weston, ACT 2611, Australia

<sup>2</sup>Department of Physics, University of Bristol, Tyndall Avenue, Bristol, BS8 1TL, UK

<sup>3</sup>European Southern Observatory, Karl-Schwarzschild-Str. 2, 85748 Garching, Germany

<sup>4</sup>Department of Physics and Astronomy, The Johns Hopkins University, 3400 North Charles Street, Baltimore, MD 21218, USA

Accepted ..... Received .....

## ABSTRACT

We recover the joint and individual space density and surface brightness distribution(s) of galaxies from the Millennium Galaxy Catalogue. The MGC is a local survey spanning  $30.9 \text{ deg}^2$  and probing approximately one–two mag arcsec<sup>-2</sup> deeper than either the Two-Degree Field Galaxy Redshift Survey (2dFGRS) or the Sloan Digital Sky Survey (SDSS). The MGC contains 10 095 galaxies to  $B_{\text{MGC}} < 20$  mag with 96 per cent spectroscopic completeness. For each galaxy we derive individual  $K$ -corrections and seeing-corrected sizes. We implement a joint luminosity-surface brightness step-wise maximum likelihood method to recover the bivariate brightness distribution (BBD) inclusive of most selection effects. Integrating the BBD over surface brightness we recover the following Schechter function parameters:  $\phi^* = (0.0177 \pm 0.0015)h^3 \text{ Mpc}^{-3}$ ,  $M_{B_{\text{MGC}}}^* - 5 \log h = (-19.60 \pm 0.04) \text{ mag}$  and  $\alpha = -1.13 \pm 0.02$ . Compared to the 2dFGRS (Norberg et al. 2002) we find a consistent  $M^*$  value but a slightly flatter faint-end slope and a higher normalisation, resulting in a final luminosity density  $j_{b,j} = (1.99 \pm 0.17) \times 10^8 h L_{\odot} \text{ Mpc}^{-3}$  — marginally higher than, but consistent with, the earlier 2dFGRS (Norberg et al. 2002), ESP (Zucca et al. 1997), and SDSS  $z = 0.1$  (Blanton et al. 2003a) results. The MGC is inconsistent with the SDSS  $z = 0$  result ( $+3\sigma$ ) if one adopts the derived SDSS evolution (Blanton et al. 2003a).

The MGC surface brightness distribution is a well bounded Gaussian at the  $M^*$  point with  $\phi^* = (3.5 \pm 0.1) \times 10^{-2} h^3 \text{ Mpc}^{-3}$ ,  $\mu^{e*} = (21.90 \pm 0.01) \text{ mag arcsec}^{-2}$  and  $\sigma_{\ln R_e} = 0.35 \pm 0.01$ . The characteristic surface brightness for luminous systems is invariant to  $M_{B_{\text{MGC}}} - 5 \log h \approx -19$  mag faintwards of which it moves to lower surface brightness. The surface brightness distribution also broadens ( $\sigma_{\ln R_e} \approx 0.5 - 0.7$ ) towards lower luminosities. The luminosity dependence of  $\sigma_{\ln R_e}$  provides a new constraint for both the theoretical development (Dalcanton, Spergel & Summers 1997; Mo, Mao & White 1998) and numerical simulations (e.g., Cole & Lacey 1996) which typically predict a mass-independent  $\sigma_{\ln R_e} \approx 0.56 \pm 0.04$  (see Vitvitska et al. 2002 and Bullock et al. 2001).

Higher resolution (FWHM  $\ll 1$  arcsec) and deeper ( $\mu_{\text{lim}} \gg 26$  mag arcsec<sup>-2</sup> in the  $B$ -band) observations of the local universe are now essential to probe to lower luminosity and lower surface brightness levels.

**Key words:** galaxies: general – galaxies: fundamental parameters – galaxies: luminosity function, mass function – galaxies: formation – galaxies: evolution – astronomical data bases: catalogues

## 1 INTRODUCTION

The recognised convention for representing the overall galaxy population is the luminosity distribution or space density of galaxies (see review by Binggeli, Sandage & Tammann 1988 and more re-

cently Driver & De Propris 2003). This distribution is typically derived from a magnitude limited redshift survey which is corrected for Malmquist bias (e.g., Efstathiou, Ellis & Peterson 1988) and fitted with the three parameter Schechter function (Schechter 1976). Generally, the Schechter function is found to be a formally good representation, although some surveys (e.g., Zucca et al. 1997; Marzke et al. 1998) have hinted at an upturn at the faintest lim-

\* E-mail: spd@mso.anu.edu.au

† PPARC Visiting Fellow

its,<sup>1</sup> where the statistics become poor (typically  $M_B - 5 \log h \approx -16$  mag, see also Blanton et al. 2005a). The process of fitting a luminosity function (LF) reduces the galaxy population to three crucial numbers: the characteristic luminosity,  $M^*$  (or  $L^*$ ), the normalisation,  $\phi^*$ , and the faint-end slope,  $\alpha$ .

Since the pioneering work of Davis & Huchra (1982) numerous measurements of these three crucial parameters have been made (see Liske et al. 2003). Among the most recent are those derived from the Two-Degree Field Galaxy Redshift Survey (2dFGRS; Norberg et al. 2002) and the Sloan Digital Sky Survey (SDSS1&2; Blanton et al. 2001; 2003a). However, although individual surveys yield Schechter function parameters to high accuracy, a comparison between independently published values shows excessively large variations, indicative of strong systematic errors (see Cross et al. 2001; Liske et al. 2003; de Lapparent 2003). Cross & Driver (2002) discuss the impact of surface brightness selection effects on measurements of the LF (see also Sprayberry et al. 1997; Dalcanton 1998) and find that such effects *may* provide an explanation for the variation seen. In Liske et al. (2003) we compared a number of recent  $B$ -band Schechter function values and used the precision number counts of the Millennium Galaxy Catalogue – with a uniform isophotal detection limit of  $26 \text{ mag arcsec}^{-2}$  in the  $B$ -band – to revise the normalisation parameters. This resulted in a reasonably consistent global Schechter function with:  $M_{b_j}^* - 5 \log h = (-19.64 \pm 0.08) \text{ mag}$ ,  $\phi^* = (1.64 \pm 0.005) \times 10^{-2} h^3 \text{ Mpc}^{-3}$  and  $\alpha = -1.1 \pm 0.1$  (taken from Driver & De Propris 2003).

Despite the apparent convergence brought about by Liske et al. (2003) there are two strong reasons to now go beyond the monivariate Schechter function:

(1) Numerical and semi-analytic simulations are sufficiently developed that it is now possible to predict not just the luminosity distribution but also the size distribution (see e.g. Mo et al. 1998; Buchalter, Jimenez & Kamionkowski 2001; Shen et al. 2003) and hence the *bivariate* distribution of luminosity and size (or luminosity and surface brightness, see e.g. Sodr e & Lahav 1993; Boyce & Phillipps 1995; de Jong & Lacey 2000; Cross & Driver 2002). This bivariate brightness distribution (BBD) can be fitted by a 6-parameter Chołoniewski function (Chołoniewski 1985) – essentially a Schechter function with a luminosity dependent Gaussian distribution in surface brightness (see e.g. de Jong & Lacey 2000; Cross & Driver 2002) – or compared directly without confinement by any functional form. Either way, a multivariate distribution provides a more stringent constraint than the monivariate Schechter function (see also Driver 2004);

(2) Liske et al. (2003) essentially circumvent the surface brightness issues raised by Cross & Driver (2002) by allowing the normalisation of the LFs to accommodate the missing flux from low surface brightness galaxies. This approximation succeeds because the galaxies that dominate the bright galaxy number counts are all around the  $L^*$  value, where the surface brightness distribution appears well defined (see Driver 1999, Cross et al. 2001). We also know from studies of giant ellipticals (Kormendy 1977; Graham & Guzman 2003), disk galaxies (de Jong & Lacey

2000), dwarf galaxies in the local group (Mateo 1998), rich clusters (Ferguson & Binggeli 1994; Andreon & Cullandre 2002) and from early work on the global field BBD (Driver 1999; Cross et al. 2001; Blanton et al. 2001; Shen et al. 2003) that there exists a luminosity surface brightness relation (see also Bell et al. 2003 for the near-IR relation and a discussion of its variation with wavelength). Together these imply that the impact of surface brightness selection effects will be a function of luminosity. Therefore recovering the full luminosity distribution can only be done by simultaneously considering luminosity *and* surface brightness – a conclusion reached many times over the past half-century (Zwicky 1957; Disney 1976; Impey & Bothun 1997).

An additional motivation is that given the size of contemporary datasets, it becomes logical to start to explore multivariate distributions to quantify trends such as the luminosity-surface brightness relation (Driver 1999) or the colour-luminosity relation (e.g., Baldry et al. 2004; see also Blanton et al. 2003b).

Here we reconstruct the bivariate luminosity-surface brightness distribution with careful attention to the impact of surface brightness and size selection effects. In Section 2 we describe the imaging and redshift data. In Section 3 we describe the conversion of our catalogue from apparent to absolute properties, the various selection boundaries and our methodology for deriving the joint luminosity-surface brightness distribution. We apply it to our data in Section 4 and compare our results to previous estimates of the BBD (de Jong & Lacey 2000; Cross et al. 2001), the LF (Norberg et al. 2002; Zucca et al. 1997; Blanton et al. 2001; Blanton et al. 2003a) and the surface brightness or size distribution (Cross et al. 2001; Shen et al. 2003). We summarise our key results in Section 5. Throughout we assume  $\Omega_o = 0.3$ ,  $\Omega_\Lambda = 0.7$  as defined in Section 3.1.

## 2 DATA

### 2.1 Photometric catalogue

The Millennium Galaxy Catalogue (MGC) is a deep ( $\mu_{\text{lim}} = 26 \text{ mag arcsec}^{-2}$ ), wide-field ( $30.88 \text{ deg}^2$ )  $B$ -band imaging survey obtained with the Wide Field Camera on the 2.5-m Isaac Newton Telescope. The survey region is a long, 35-arcmin wide strip along the equator, covering from  $9^{\text{h}}58^{\text{m}}28^{\text{s}}$  to  $14^{\text{h}}46^{\text{m}}45^{\text{s}}$  (J2000), and is fully contained within the regions of both the 2dFGRS and SDSS Data Release 1 (DR1; Abazajian et al. 2003).

In Liske et al. (2003) we gave a detailed description of the observations, reduction, object detection, Galactic extinction correction and classification (using SExtractor; Bertin & Arnouts 1996) and presented precision galaxy number counts over the range  $16 \leq B_{\text{MGC}} < 24 \text{ mag}$ . All non-stellar sources to  $B_{\text{MGC}} = 20 \text{ mag}$  were visually inspected and if an object was found to be incorrectly deblended or if the object’s parameters were obviously wrong, the object was re-extracted by manually changing the SExtractor extraction parameters until a satisfactory result was achieved. In addition, all low-quality regions in the survey (e.g. near CCD defects) were carefully masked out (see Liske et al. 2003 and Lemon et al. 2004). We demonstrated that the internal photometric accuracy of the MGC is  $\pm 0.023 \text{ mag}$  and that the astrometric accuracy is  $\pm 0.08 \text{ arcsec}$ . In Cross et al. (2004) we then compared the photometric accuracy, completeness and contamination of the MGC to the 2dFGRS and SDSS-EDR and DR1 datasets. Being deeper and of higher resolution, we found that the MGC is both more accurate and more complete than either of these surveys. The MGC is currently the highest quality and most complete representation of the

<sup>1</sup> It is worth noting that the luminosity distributions seen in rich clusters such as A963, Coma and Virgo are also seen to turn up at a similar magnitude, (see e.g. Driver et al. 1994; Trentham 1998; Driver, Couch & Phillipps 1998; Driver & De Propris 2003; and (Popesso et al. 2004)). Conversely the local group luminosity function remains flat to the Jeans mass limit (Karachentsev et al. 2003).

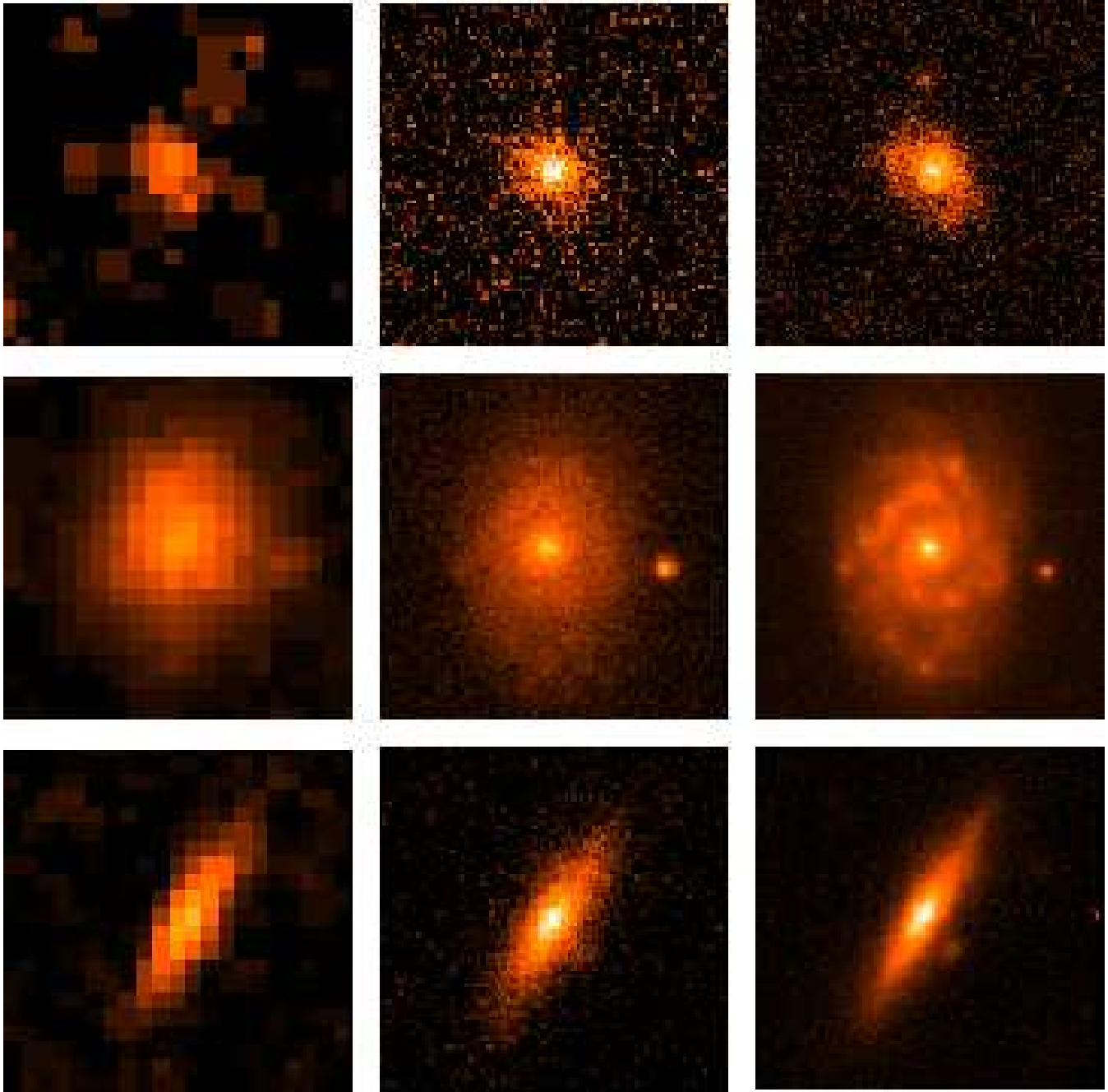


**Figure 1.** A comparison between Digital Sky Survey (left panels,  $b_J$ -band), SDSS-DR1 (centre,  $g$ -band) and MGC (right panels) images: MGC03494 (upper); MGC18325 (middle); MGC04795 (lower). The data illustrate the greater depth and higher resolution of the MGC. All images are  $33''$  on each side and scaled to comparable dynamic ranges. Figure degraded see <http://www.eso.org/~jliske/mgc/> for full pdf copy of this paper.

nearby galaxy population. Fig. 1 shows images of three galaxies from the Digital Sky Survey (left), the SDSS (centre) and the MGC (right), illustrating the superior resolution and greater depth of the MGC data.

The MGC-BRIGHT catalogue of Liske et al. (2003) was bounded at the bright end by 16 mag, where stars begin to flood in our best seeing fields. We now extend this catalogue brightwards to  $B_{\text{MGC}} = 13$  mag by carefully examining all non-stellar objects in the range  $13 \leq B_{\text{MGC}} < 16$  mag, repairing objects that had been over-deblended by SExtractor and checking completeness with NED at  $B_{\text{MGC}} < 15$  mag, where SExtractor – op-

timised for faint galaxy detection and photometry – may occasionally miss very large objects. A second change to MGC-BRIGHT with respect to Liske et al. (2003) is the deletion of some exclusion regions. Liske et al. had placed exclusion regions around very bright objects ( $B_{\text{MGC}} < 12.5$  mag) to avoid spurious halo detections and problems with background estimation in their vicinity. 20 such regions had been erroneously placed around galaxies fainter than 12.5 mag and these have been deleted, resulting in an increase of the good-quality survey area from 30.84 to 30.88 deg<sup>2</sup>.

Further minor changes were introduced to MGC-BRIGHT, each affecting ~tens of objects: different deblending decisions;

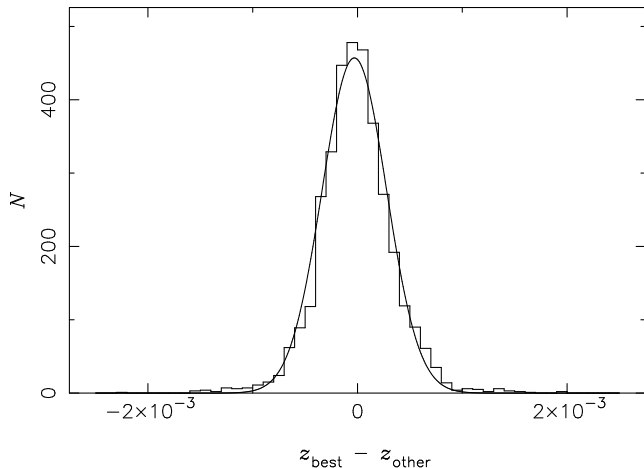


**Figure 2.** Histogram of redshift differences for 2709 objects with multiple redshift measurements. The distribution has an rms dispersion of  $92 \text{ km s}^{-1}$ . The solid line is a Gaussian with the same median and rms as the data.

spectroscopic identification of galaxies previously misclassified as stars (compact emission line galaxies) and vice versa (stars which appear extended because of almost perfect alignment with small, faint background galaxies); and identification of asteroids previously misclassified as galaxies (discovered by comparison with SDSS-DR1 imaging data).

The final MGC-BRIGHT sample now comprises 10 095 galaxies.

## 2.2 Redshifts

### 2.2.1 Publicly available data

By design the MGC survey region is fully contained within the 2dFGRS and SDSS survey regions. Hence we first turned to these surveys in order to obtain redshifts for MGC-BRIGHT. In addition we obtained redshifts from the 2QZ (Croom et al. 2001), NED (excluding 2dFGRS and SDSS objects) and the smaller surveys of Francis, Nelson & Cutri (2004) (PF) and Impy et al. (1996) (LSBG). In turn each survey,  $X$ , was matched against MGC galaxies and stars with  $B_{\text{MGC}} < 22$  mag. This magnitude limit and the following matching procedure were chosen in order to be able to account for every  $X$  object and hence to verify the completeness of the MGC.

First we found all pairs of  $X$  and MGC objects where each is identified as the other’s nearest neighbour in that catalogue. A pair with separation  $d$  smaller than some  $d_{\text{cut}}$  is classified as a match unless one or more other MGC objects have also identified the  $X$  object as their nearest neighbour in  $X$  with a separation  $< 2.5d$  (where  $d$  refers to the separation of the closest pair). These  $X$  objects as well as objects with  $d \geq d_{\text{cut}}$  and those which have not been identified as a nearest neighbour by any MGC objects are classified as initially unmatched. The value of  $d_{\text{cut}}$  is chosen as the separation where the invariably occurring tail in the distribution of separations begins to dominate.

The above definition of initially unmatched objects is designed to conservatively flag all possible mismatches. Almost all mismatches fall into one of three categories, which are a priori difficult to distinguish from one another but for which one needs to proceed differently: (i) unusually large positional disagreement; (ii) two (or more) objects in one catalogue where the other catalogue only has

one object, because of different deblending choices or different resolution; (iii) one object in  $X$  but none in MGC because of inaccurate photometry in either  $X$  or MGC, or because the  $X$  object is an asteroid or a spurious noise detection, or because the object is genuinely missing from the MGC.

All initially unmatched objects are visually inspected in order to reliably identify those objects that were in fact correctly matched. The few cases where the mismatch was due to poor object extraction in the MGC were fixed.

Each redshift of a matched object is assigned a redshift quality,  $Q_z$ , which has the same meaning as in the 2dFGRS (Colless et al. 2001):  $Q_z = 1$  means no redshift could be measured;  $Q_z = 2$  means possible but doubtful redshift;  $Q_z = 3$  means probable redshift; and  $Q_z = 4$  or 5 means good or very good redshift.  $Q_z = 1$  and 2 are considered failures and we will use only redshifts with  $Q_z \geq 3$  in this paper. In addition to the 2dFGRS this system is also already used by PF. We translate the various quality parameters of the other surveys to our system in the following manner: SDSS-DR1 redshifts are assigned  $Q_z = 4$  unless the SDSS ZStatus or ZWarning flags indicate a serious problem; for the 2QZ we use  $Q_z = 5 - Q(2QZ)$ ; and NED and LSBG redshifts are assigned  $Q_z = 3$ .

In total the public data provided good quality redshifts for 4804 MGC galaxies.

### 2.2.2 MGCz

In order to complete the redshifts for the full MGC-BRIGHT sample we conducted our own redshift survey (which we label MGCz), targeting those galaxies which did not already have publicly available redshifts. These observations were mainly carried out with the Two Degree Field (2dF) facility on the Anglo Australian Telescope. The data were collected, reduced and redshifted in an identical manner to that of the 2dFGRS (see Colless et al. 2001 for full details). In particular we again used the same redshift quality parameter,  $Q_z$ , as the 2dFGRS (see above).

The redshift incompleteness of the 2dF data showed a clear bias against low-surface brightness galaxies. Hence we undertook additional single-object long-slit observations, targeting low-surface brightness galaxies ( $\mu_{\text{app}}^e > 24 \text{ mag arcsec}^{-2}$ , where  $\mu_{\text{app}}^e$  is the apparent effective surface brightness within the half-light radius, see Section 3.4) as well as gaps in our 2dF coverage, with the Double Beam Spectrograph (DBS) on the Australian National University’s 2.3-m, the Low Resolution Spectrograph (LRS) on the 3.6-m Telescopio Nazionale Galileo on La Palma, the ESO Multi-Mode Instrument (EMMI) on the New Technology Telescope in La Silla and the Gemini Multiple Object Spectrograph (GMOS, long-slit nod & shuffle mode) on Gemini North. In all cases we observed between 600 and 3600 s through a 1.5 to 2-arcsec wide slit, aligning the slit with the major axis of the object to collect as much flux as possible. All the data were reduced in a similar manner using standard IRAF procedures. The resulting spectra are of similar resolution as our 2dF data, but of higher quality: they increased our redshift completeness at  $B_{\text{MGC}} < 19.5$  mag and  $\mu_{\text{app}}^e > 24 \text{ mag arcsec}^{-2}$  from 90.7 to 98.8 per cent.

### 2.2.3 Combined redshift sample

Using all available data and MGCz data the overall redshift completeness of MGC-BRIGHT is 96.05 per cent. In Fig. 3 (third row from top) we show the final incompleteness as a function of apparent effective surface brightness and apparent magnitude,  $(g-r)$  and

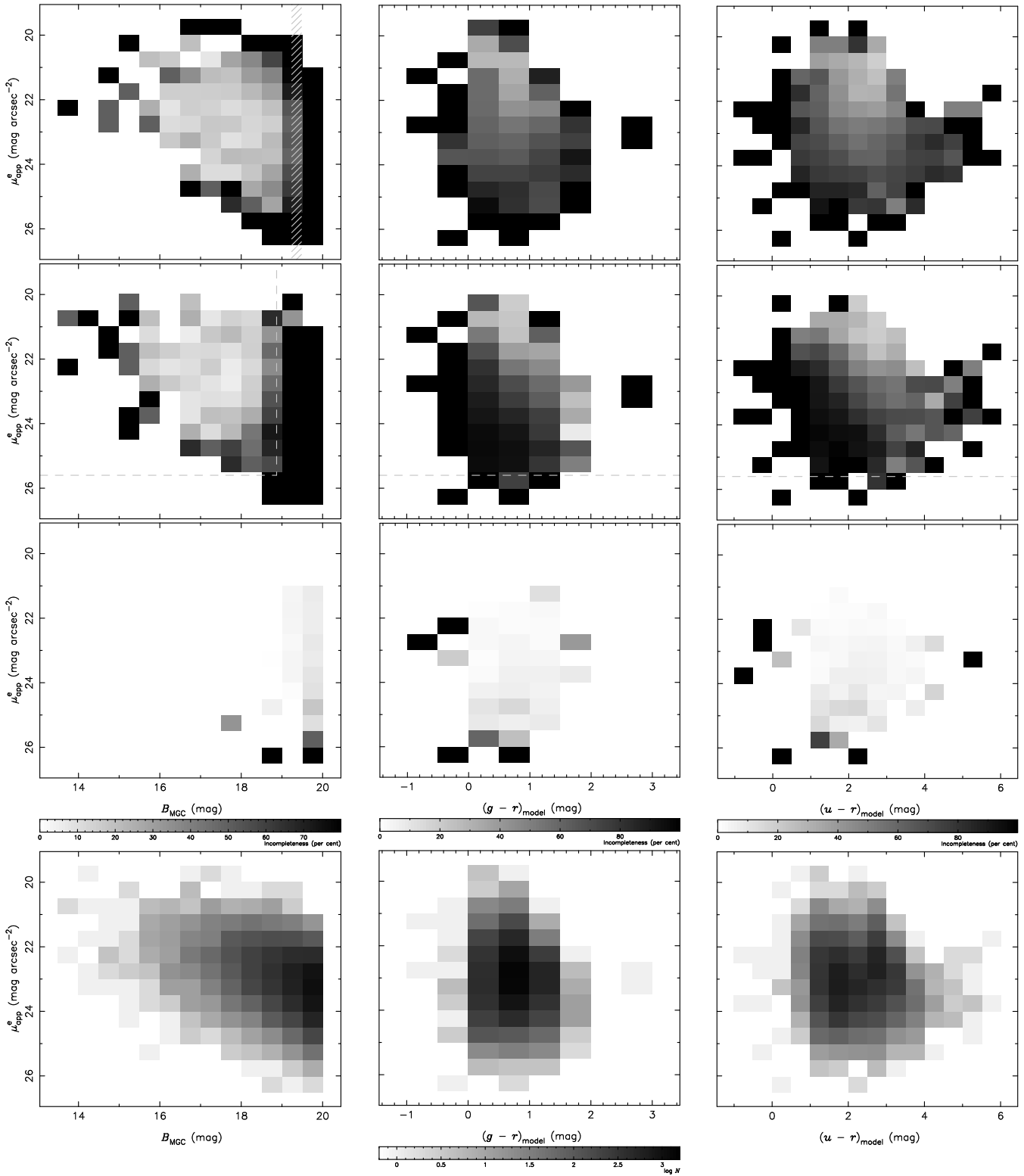


**Figure 3.** Top row: the redshift incompleteness for the 10 095 galaxies in the 30.88 deg $^2$  MGC region using only 2dFGRS redshifts as a function of apparent effective surface brightness and apparent magnitude (left),  $(g-r)$  (centre) and  $(u-r)$  colour (right). The second row shows the same using only SDSS redshifts. These figures demonstrate the significant contributions of these surveys to our final redshift catalogue (third row) which has an overall completeness of 96.05 per cent. The light hashed region in the top left panel marks the approximate magnitude limit of the 2dFGRS, which varies as a function of position on the sky. The dashed lines in the second row mark the approximate SDSS spectroscopic magnitude and surface brightness limits. No galaxies beyond these respective limits were targeted by these surveys. The bottom row shows the number of objects per bin.

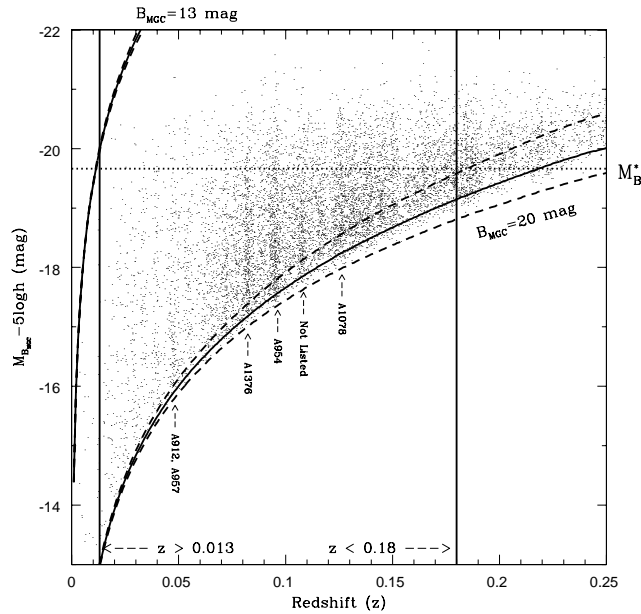


**Figure 4.** Absolute magnitude versus redshift for the MGC using the individual  $K$ -corrections as defined in Section 3.2. The solid curves show the bright and faint magnitude limits assuming the mean  $K$ -correction and a universal evolution of  $L = L_0(1+z)^{0.75}$ . The dashed lines again show the magnitude limits but now assuming the bluest and reddest  $K$ -corrections used in the MGC. The upper and lower redshift limits are marked as vertical lines and the  $M_B^*$  value from Norberg et al. (2002) is shown as a horizontal dotted line. Note that the lower redshift limit defines the minimum absolute magnitude of  $M_B - 5 \log h = -13$  mag. The locations of known Abell clusters are indicated and clearly show up as redshift over-densities.

( $u - r$ ) model colours. In Table 1 we list the numbers of redshifts contributed by each of the surveys.

For 2709 galaxies we have more than one  $Q_z \geq 3$  redshift measurement, totaling 6226 redshifts. These duplications are mainly due to overlaps between the 2dFGRS and SDSS-DR1, but 232 of these galaxies have at least one MGCz redshift. For these objects we pick a ‘best’ redshift by sorting first by  $Q_z$ , then by signal-to-noise ratio (where available) and then by the order of the surveys in Table 1. Fig. 2 shows the distribution of differences between the multiple redshifts which has an rms of  $92 \text{ km s}^{-1}$ .

### 3 COSMOLOGY, $K$ -CORRECTIONS, EVOLUTION, SELECTION LIMITS AND ANALYSIS METHOD

To calculate the MGC BBD we first need to adopt a cosmological framework, appropriate  $K$ -corrections [ $K(z)$ ] and an evolutionary model [ $E(z)$ ]. It is of course possible to determine a LF while simultaneously solving for one or more of these quantities – see e.g. Blanton et al. (2003a), who derive a LF while simultaneously solving for both the number-density evolution and the luminosity evolution. However, our concern with this approach is that it can lead to erroneous results *if* the incompleteness is significant and biased (as indicated in Cross et al. 2004 and Fig. 3). In this case the evolutionary functions would be fitting not only evolution but also the uncorrected selection biases. Instead, our philosophy is to adopt reasonable assumptions for the evolution and concentrate on a strategy to account for selection bias.

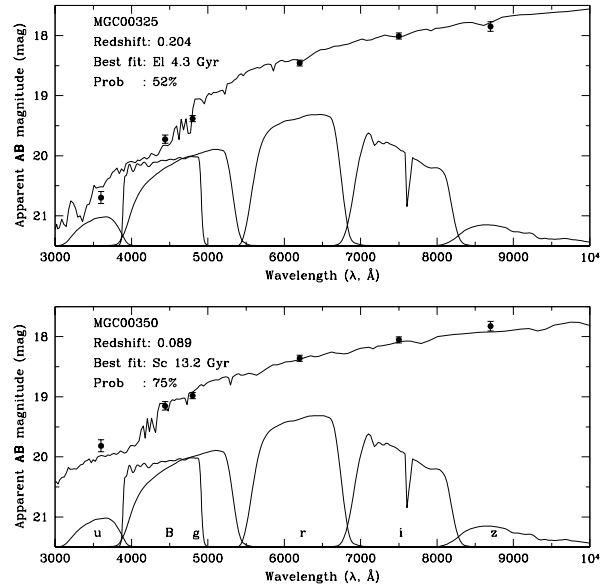


**Figure 5.** Two examples of our spectral fitting algorithm, indicating a good match to a young elliptical (upper panel) and older late-type (lower). Once the optimum spectrum has been determined this is used to determine the  $B_{\text{MGC}}$ -band  $K$ -correction.

### 3.1 Cosmology

We use  $\Omega_0 = 0.3$  and  $\Omega_\Lambda = 0.7$  – broadly confirmed by the WMAP mission combined with the 2dFGRS power spectrum – but adopt  $h = H_0/(100 \text{ km s}^{-1} \text{ Mpc}^{-1})$  for ease of comparison with previous results. We also define maximum and minimum redshift limits. The maximum limit is chosen as the point at which red  $L^*$ -galaxies fall below our imposed  $B_{\text{MGC}} = 20$  mag limit (this occurs at  $z_{\text{MAX}} = 0.18$ , see Fig. 4, excluding 1774 galaxies). The lower limit is determined by the point at which the redshifts are significantly influenced by the local velocity field. From Peacock et al. (2001) we find that the pairwise velocity dispersion, as measured from the 2dFGRS, is  $385 \text{ km s}^{-1}$ . Hence to ensure minimal impact from peculiar velocities (i.e.,  $v_{\text{Peculiar}} < 0.1v_{\text{Recession}}$ ) we must set  $z_{\text{MIN}} = 0.013$  (excluding 44 galaxies). Fig. 4 shows the absolute magnitude versus redshift distribution for our data along with the upper and lower redshift limits (vertical lines) and the typical value of  $M_B^*$  (Norberg et al. 2002; dotted line). Note that the lower  $z$  limit, combined with the faint apparent magnitude limit ( $B_{\text{MGC}} = 20$  mag) ultimately defines how far down the luminosity distribution one can probe ( $M_B - 5 \log h \approx -13$  mag). One can only *reliably* push fainter by extending the faint apparent magnitude limit of the survey and not by covering a wider area (unless direct distances are measured or the detailed local peculiar velocity field is modeled). In total there are 7878 galaxies within these redshift limits.

### 3.2 The $K$ -correction

$K$ -corrections, or bandpass corrections, are galaxy specific – ultimately galaxy component specific – and given the known variation in galaxy types, a mean  $K$ -correction (as adopted in Norberg et al. 2002 and in most previous studies) may be overly simplistic (see also Blanton et al. 2003a who reach a similar con-

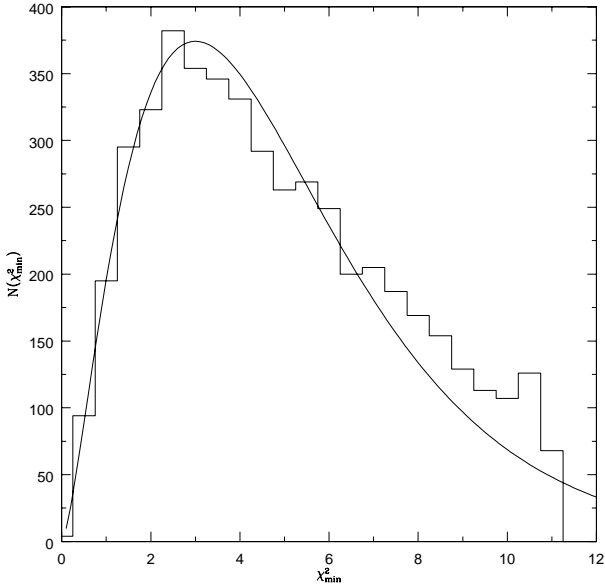


**Figure 6.** The resulting  $\chi_{\min}^2$ -probability distribution from our  $K(z)$  fitting algorithm (histogram) as compared to the expected distribution (for five degrees of freedom, solid line). Note that because we re-analyse galaxies with probabilities less than 5 per cent no values with  $\chi_{\min}^2 \geq 11$  occur.

clusion). Here we identify a best fit synthetic spectrum from the combined broad-band MGC and SDSS-DR1 colours for each individual galaxy and then directly measure the  $K$ -correction from this optimal template. We use the extinction-corrected MGC Kron (2.5 Kron radii) and extinction-corrected SDSS-DR1 Petrosian magnitudes for this purpose. The Petrosian magnitudes are corrected to the AB system using  $u_{AB} = u_{SDSS} - 0.04$ ;  $g, r, i_{AB} = g, r, i_{SDSS}$  and  $z_{AB} = z_{SDSS} + 0.02$  as recommended on the SDSS-DR2 website. The  $B_{MGC}$  magnitudes are adjusted for the known zeropoint offset of 0.039 mag between the MGC and SDSS-DR1 (Cross et al. 2004) and converted from Vega to AB. This conversion was found to be  $B_{MGC}(AB) = B_{MGC}(Vega) - 0.118$  for the MGC system.

We now wish to derive the optimal spectral template match to these six filters in the AB system. We elect to use the spectrum library of Poggianti (1997) which includes ellipticals and early and late-type spirals, with ages ranging from 15 Gyr to 3.7 Gyr (27 synthetic templates in all). To determine the best template we calculate the AB magnitudes as if observed through the  $B_{MGC}$  and SDSS  $u, g, r, i, z$  filters for a single template and iteratively rescale the amplitude of the spectral template to minimise  $\chi^2$ :

$$\chi^2 = \sum_{x=u,B,g,r,i,z} \left[ \frac{(x - x_{\text{MODEL}})}{\Delta x} \right]^2$$

Where the errors are given by:  $\Delta u = \pm 0.10$ ;  $\Delta B = \pm 0.07$ ;  $\Delta g = \pm 0.05$ ;  $\Delta r = \pm 0.05$ ;  $\Delta i = \pm 0.05$  and  $\Delta z = \pm 0.08$  mag. These error values were derived as follows. Firstly, using just the SDSS filters, we determined the  $\chi_{\min}^2$ -distribution for the optimal spectral fits based on the errors listed on the SDSS website ( $\Delta u = \pm 0.1$  [red leak],  $\Delta gri = \pm 0.02$ ,  $\Delta z = \pm 0.03$ ). We then scaled the  $gri z$  errors until the recovered  $\chi_{\min}^2$ -distribution matched the expected distribution for four degrees of freedom. We then repeated this process now including the  $B_{MGC}$  filter (see Fig. 6). These final errors are in good agreement with the study of Cross et al. (2004).

The  $\chi^2$ -minimisation was repeated for each of the 27 spectral templates and the smallest of the 27  $\chi_{\min}^2$  values used to iden-

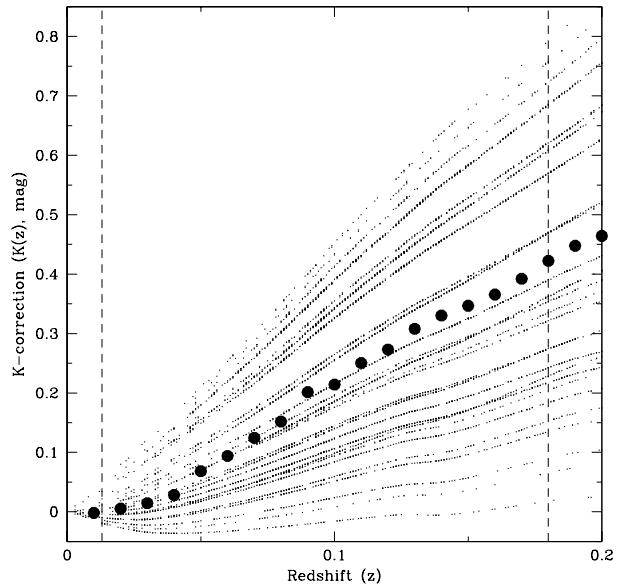


**Figure 7.** Our final  $K$ -corrections. The MGC  $K$ -corrections trace out the 27 tracks of the synthetic spectra of Poggianti (1997). The filled circles indicate the mean of our data and the vertical dashed lines show the adopted redshift limits used in the BBD analysis.

tify the most appropriate template. Finally if the  $\chi_{\min}^2$ -probability for the optimal template was less than 5 per cent we repeated the process, first rejecting the  $B_{MGC}$  filter and then the  $u$  and  $z$  filters in turn (hence the truncation at  $\chi_{\min}^2 \approx 11$  on Fig. 6). Magnitudes fainter than the quoted 95 per cent completeness limit were not used ( $u = 22.0$ ,  $g = 22.2$ ,  $r = 22.2$ ,  $i = 21.3$ ,  $z = 20.5$  mag, see Abazajian et al. 2003). Fig. 5 shows two example galaxies with the best-fit spectral templates overlaid on the measured magnitudes. Fig. 6 shows the resulting  $\chi_{\min}^2$  distribution (histogram) and the expected  $\chi^2$ -distribution (for five degrees of freedom, solid line).

Shown in Fig. 7 are the resulting  $K$ -corrections for the MGC, which trace out the 27 different spectral templates, as well as the mean  $K$ -correction in 0.01 redshift intervals (large dots). Finally, in the few cases (25 galaxies in total) where a galaxy did not have an SDSS-DR1 match we assigned the mean  $K$ -correction value at the galaxy's redshift.

### 3.3 Evolution

We adopt a global evolution of the form  $L = L_0(1+z)^\beta$  with an initial value of  $\beta = 0.75$  (i.e.,  $E(z) = -0.75 \times 2.5 \log(1+z)$ , see Phillipps & Driver 1995). Given the redshift limits this implies an evolutionary correction in the range 0.01 – 0.14 mag. This is a passive luminosity evolution model with no merging over this redshift range ( $0.013 < z < 0.18$ ). In Section 4.3 we solve for  $\beta$  and find  $-2.0 < \beta < 1.25$  (see Fig. 20). More complex evolutionary scenarios will be considered in future papers where we subdivide the galaxy population by type and component. However we do note that recent studies (e.g., Patton et al. 2000) including our own (De Propris et al. 2005) indicate a very low low- $z$  merger rate based on counts of dynamically close pairs. It is also worth noting that the step-wise maximum likelihood method used assumes no number density evolution.

### 3.4 Estimating MGC effective surface brightnesses

We adopt the effective surface brightness, i.e. the average surface brightness within the half-light radius, as our structural measurement. The effective surface brightness is chosen as it makes no assumption of the radial flux profile and can be measured empirically from the data for any galaxy shape. Hence it is a direct measure reflecting the global compactness regardless of whether the galaxy is smooth or lumpy.

The half-light radius is the semi-major axis of the ellipse containing half the flux of SExtractor’s BEST magnitude. The ellipse’s centre, ellipticity and position angle are taken from SExtractor. For compact objects the half-light radius is affected by the seeing. Through simulations of both exponential and de Vaucouleurs profile galaxies using IRAF ARTDATA (see Appendix A for details) we find that we can correct the observed half-light radius for this blurring and recover its true value,  $r_e^0$ , to an accuracy of 10 per cent (see Fig. A2) by:

$$r_e^0 = \sqrt{r_e^2 - 0.32 \Gamma^2}, \quad (1)$$

where  $r_e$  is the observed half-light radius and  $\Gamma$  is the FWHM of the seeing profile, all in arcsec.

Work is currently underway to determine 2D bulge-disk decompositions from the MGC data which will be presented in a future paper. However at this stage it is unclear whether the effective radius or independent bulge and disk parameters are the more fundamental. Here, we define our absolute effective surface brightness,  $\mu^e$ , as:

$$\mu^e = B_{\text{MGC}} + 2.5 \log[2\pi(r_e^0)^2] - 10 \log(1+z) - K(z) - E(z), \quad (2)$$

We note that  $r_e^0$  is defined along the semi-major axis and hence the above prescription assumes galaxies are optically thin, i.e., derived parameters are independent of inclination. The role of dust will be explored in a future paper.

### 3.5 Selection limits

Like all surveys our catalogue will suffer from some level of incompleteness in both the imaging and spectroscopic surveys. As our data are the deepest available over this region of sky we cannot empirically quantify our imaging incompleteness (see Cross et al. 2004 for an assessment of the incompleteness of the SuperCOSMOS Sky Survey, 2dFGRS and SDSS-EDR/DR1 relative to the MGC). We can, however, define the selection limits at any redshift, following Driver (1999), and use this information later (Section 3.6) to quantify the selection boundary in our final space density distribution.

We begin by noting the MGC’s apparent survey limits: a bright and faint apparent magnitude limit of  $m_{\text{BRIGHT}} = 13$  mag and  $m_{\text{FAINT}} = 20$  mag, a limiting apparent effective surface brightness of  $\mu_{\text{LIM}}^e = 25.25$  mag arcsec $^{-2}$ , a minimum size of  $r_{\text{MIN}} = (0.04\Gamma^2 + 0.37\Gamma + 0.1)^{\frac{1}{2}}$  arcsec (where  $\Gamma$  is the seeing FWHM) and a maximum size of  $r_{\text{MAX}} = 15$  arcsec. The last three limits refer to the seeing-corrected quantities (see Section 3.4) and were derived from simulations of 45°-inclined optically thin exponential disks using IRAF’s ARTDATA package (see Appendix A for details). It is important to note that the surface brightness and maximum size limits do *not* define the *absolute detection* limits but the boundary of *reliable photometry* (where ‘reliable’ is arbitrarily defined as  $\pm 0.1$  mag and  $\pm 0.1$  mag arcsec $^{-2}$  accuracy, see Fig. A2). Fig. 9 shows these limits in the apparent magnitude-apparent ef-

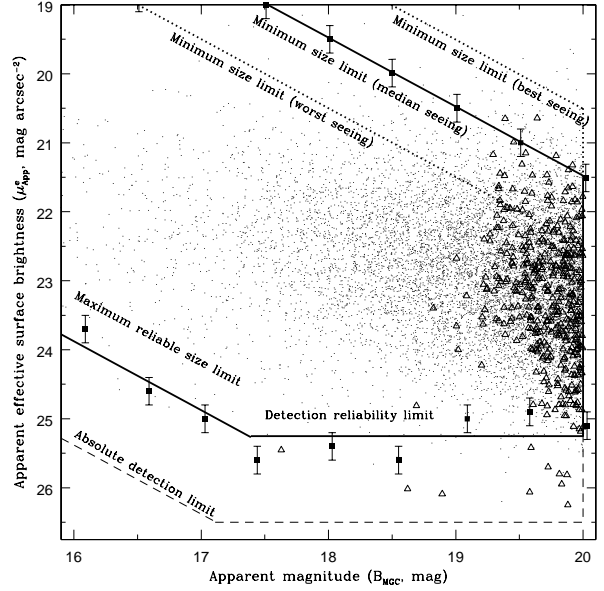


**Figure 9.** The distribution of galaxies with (dots) and without (open triangles) redshifts along with selection limits. Square data points with errorbars show the selection limits as determined from the simulations of Appendix A and the solid line shows the fit. The low surface brightness and maximum size limits are defined as limits of reliable photometry by requiring errors in the photometry of less than  $\pm 0.1$  mag and  $\pm 0.1$  mag arcsec $^{-2}$ . The dashed line is the fundamental detection limit.

fective surface brightness plane, along with the galaxy distribution with (dots) and without (triangles) redshifts.

For each galaxy  $i$  with known redshift,  $z_i$ , we can now determine the parameter space in absolute magnitude,  $M$ , and absolute effective surface brightness,  $\mu^e$ , over which this galaxy could have been observed, given the survey limits. The appropriate limits are (following Driver 1999):

$$\begin{aligned} M_{\text{BRIGHT},i} &= m_{\text{BRIGHT}} - 5 \log d_L(z_i) - 25 - K(z_i) - E(z_i) \\ M_{\text{FAINT},i} &= m_{\text{FAINT}} - 5 \log d_L(z_i) - 25 - K(z_i) - E(z_i) \\ \mu_{\text{LOW},i}^e &= \mu_{\text{LIM}}^e - 10 \log(1+z_i) - K(z_i) - E(z_i) \\ \mu_{\text{LOW},i}^e &= M_i + 5 \log d_L(z_i) + 25 + 2.5 \log(2\pi r_{\text{MAX}}^2) \\ &\quad - 10 \log(1+z_i) \\ \mu_{\text{HIGH},i}^e &= M_i + 5 \log d_L(z_i) + 25 + 2.5 \log(2\pi r_{\text{MIN}}^2) \\ &\quad - 10 \log(1+z_i) \end{aligned} \quad (3)$$

Note that  $\mu_{\text{LOW},i}^e$  is defined by both the minimum effective surface brightness for reliable detection,  $\mu_{\text{LIM}}^e$ , and the maximum reliable size limit,  $r_{\text{MAX}}$ . The maximum reliable size limit is imposed by the smoothing box size when calculating the background sky levels. These limits are introduced in more detail in Driver (1999). One can also envisage a sixth limit (also  $\mu_{\text{HIGH},i}^e$ ) due to the dynamic range of the CCD detector. In our case none of the galaxies have their central regions flooded and so this limit can be ignored.

Fig. 10 shows the selection limits for three galaxies at redshifts 0.025 (lower panel), 0.100 (middle) and 0.175 (upper) along with the location of the galaxy (large solid circle), galaxies with similar redshifts (open squares) and the full ( $0.013 < z < 0.18$ ) MGC distribution (dots). The selection boundary consistently forms a five-sided figure which glides through the full distribution as the redshift increases. Because of the individual  $K$ -corrections each



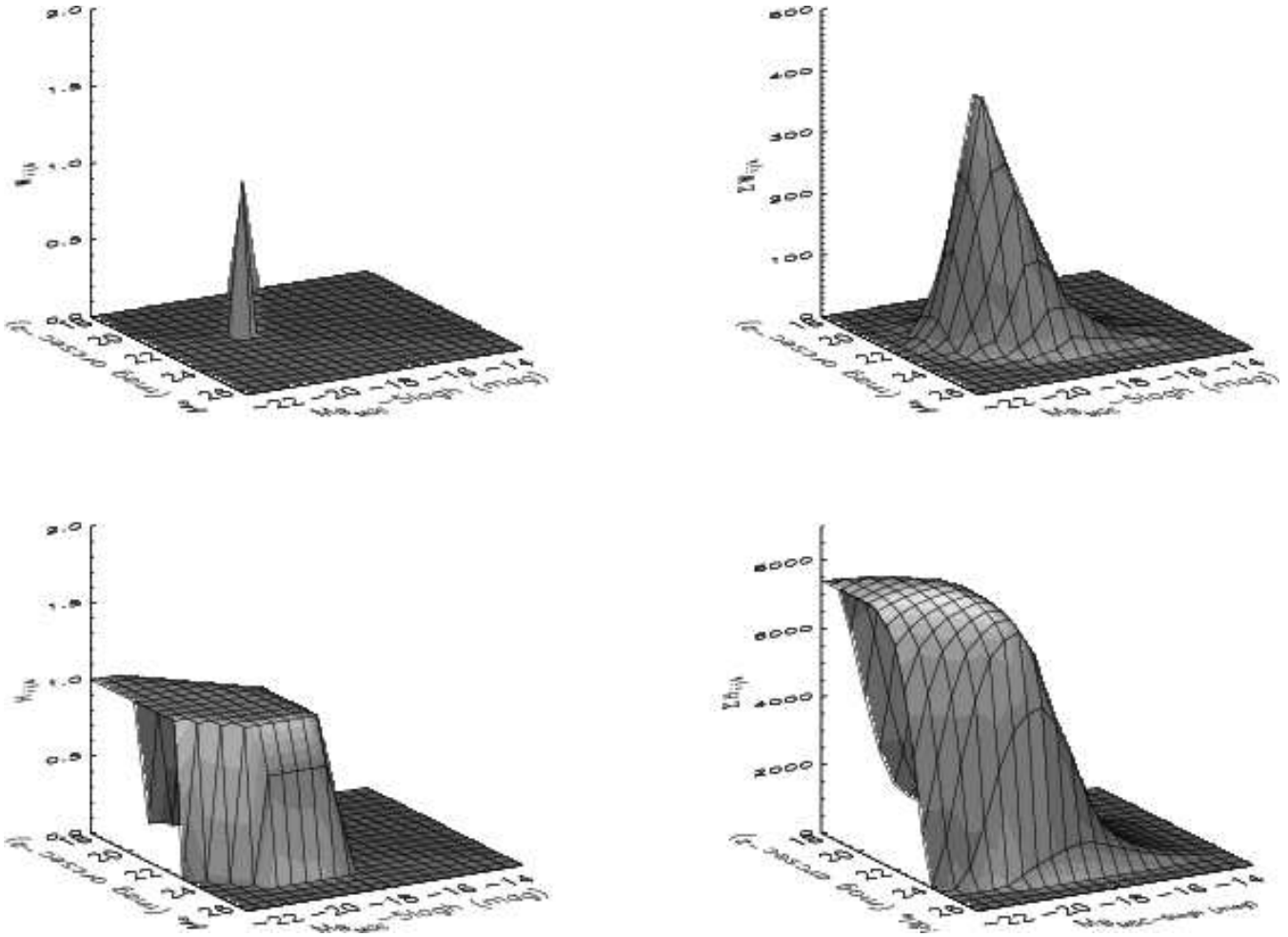


**Figure 8.** An illustration of our BBD SWMI approach. Left panels: examples of the individual matrices  $W_{ijk}$  (weighting function; upper) and  $H_{ijk}$  (pseudo-visibility function; lower) for MGC16504. Right panels:  $\sum_i W_{ijk}$  (upper) and  $\sum_i H_{ijk}$  (lower). Figure degraded see <http://www.eso.org/~jlliske/mgc/> for full pdf copy of this paper.

galaxy has its own unique selection window. It is worth noting that large luminous galaxies are undetectable, or at least photometrically unreliable, at very low redshift. Hence the methods of Shen et al. (2003) which use  $z_{\text{MEDIAN}}(M, \mu^e)$ -style corrections, may underestimate this population because they implicitly assume selection boundaries only cut into the distribution at some upper redshift limit. Cross et al. (2001) accounted for this effect in their analysis.

For each galaxy with known redshift we now define an observable window function,  $O_i(M, \mu^e)$ , as:

$$O_i(M, \mu^e) = \begin{cases} 1 & \text{if } M_{\text{BRIGHT},i} < M < M_{\text{FAINT},i} \\ & \text{and } \mu_{\text{HIGH},i}^e < \mu^e < \mu_{\text{LOW},i}^e \\ 0 & \text{otherwise.} \end{cases} \quad (4)$$

The functions  $O_i$  will be used in Section 3.6 in the construction of the BBD.

### 3.6 Bivariate step-wise maximum likelihood

We now construct the MGC BBD using a bivariate brightness step-wise maximum likelihood (SWML) estimator similar to that described by Sodr  & Lahav (1993). This is an extension of the stan-

dard SWML method defined by Efstathiou et al. (1988) in the sense that the sample is now divided into bins of both absolute magnitude *and* absolute surface brightness as opposed to just absolute magnitude alone. Note that Sodr  & Lahav (1993) formulated their method in terms of absolute magnitude and a physical diameter. However, the MGC is primarily magnitude and surface brightness limited with a fixed isophotal detection limit of 26 mag arcsec<sup>-2</sup>. For this reason we elect to work in  $M-\mu^e$  space rather than  $M-R_e$  space.

Essentially, for  $i = 1 \dots N$  objects the volume-corrected relative BBD in  $j = 1 \dots J$  absolute magnitude bins and  $k = 1 \dots K$  surface brightness bins with widths  $\Delta M$  and  $\Delta \mu^e$  can be evaluated by (cf. Sodr  & Lahav 1993):

$$\phi_{jk} = \frac{\sum_i W_{ijk}}{\sum_i [H_{ijk} / \sum_l \sum_m \bar{\phi}_{lm} H_{ilm}]}, \quad (5)$$

where the relative space density of galaxies,  $\phi_{jk}$ , is given in terms of the space density of the previous iteration,  $\bar{\phi}_{jk}$ , the weighting function,  $W_{ijk}$ , and the visibility function,  $H_{ijk}$ .

The weighting function,  $W_{ijk}$ , corrects for the incompleteness in our redshift survey. This incompleteness is demonstrably not random (see Fig. 3) and we are preferentially missing faint dim galaxies with extreme colours. When constructing LFs this bias is

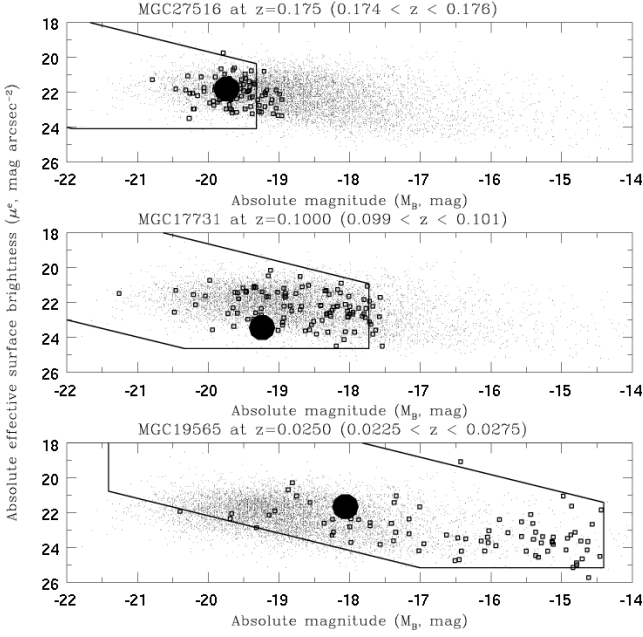


**Figure 10.** The selection boundaries for three galaxies as indicated along with the location of the galaxy (solid circle), those with similar redshifts (open squares but differing  $K$ -corrections) and the full ( $0.013 < z < 0.18$ ) MGC distribution (dots). The figure illustrates that the selection boundaries vary dramatically with redshift (bottom to top) such that each redshift slice, within the survey limitations, only samples a restricted region of the luminosity-surface brightness plane. Note that some points may lie outside the box if their  $K$ -corrections are significantly different from the galaxy for which the selection lines have been drawn. Figure degraded see <http://www.eso.org/~jlliske/mgc/> for full pdf copy of this paper.

often ignored (e.g., Blanton et al. 2003a) or considered a function of magnitude only (e.g., Norberg et al. 2002). Here, we account for luminosity and surface brightness dependent incompleteness and define  $W_{ijk}$  as:

$$W_{ijk} = \begin{cases} \frac{N_i}{N_i(Q_z \geq 3)} & \text{if } M_j - \frac{\Delta M}{2} \leq M_i < M_j + \frac{\Delta M}{2} \\ & \text{and } \mu_k^e - \frac{\Delta \mu^e}{2} \leq \mu_i^e < \mu_k^e + \frac{\Delta \mu^e}{2} \\ 0 & \text{otherwise,} \end{cases} \quad (6)$$

where  $N_i$  is the total number of galaxies lying in the same apparent magnitude-apparent surface brightness bin as galaxy  $i$  and  $N_i(Q_z \geq 3)$  is the number of galaxies with known redshifts (i.e., those with  $Q_z \geq 3$ , see Section 2) in the same bin. Hence each galaxy is weighted by the inverse of the redshift completeness in the galaxy's apparent magnitude-surface brightness bin.

The visibility function  $H_{ijk}$  is given by:

$$H_{ijk} = \frac{1}{(\Delta M \Delta \mu^e)} \int_{M_j - \Delta M/2}^{M_j + \Delta M/2} dM \int_{\mu_k^e - \Delta \mu^e/2}^{\mu_k^e + \Delta \mu^e/2} d\mu^e O_i(M, \mu^e), \quad (7)$$

where  $O_i(M, \mu^e)$  is defined in Section 3.5. Hence  $H_{ijk}$  is the fraction of the  $M_j - \mu_k^e$  bin which lies inside the observable window of galaxy  $i$ .

Fig. 8 shows example  $W_{ijk}$  and  $H_{ijk}$  matrices for  $i = \text{MGC16504}$  (upper and lower left respectively) as well as the summed  $\sum_{i=1}^N W_{ijk}$  and  $\sum_{i=1}^N H_{ijk}$  matrices (upper right and lower right respectively).  $\sum_i W_{ijk}$  is essentially the observed galaxy distribution corrected for incompleteness and  $\sum_i H_{ijk}$  is analogous to the visibility surface of Visibility Theory (Phillipps,

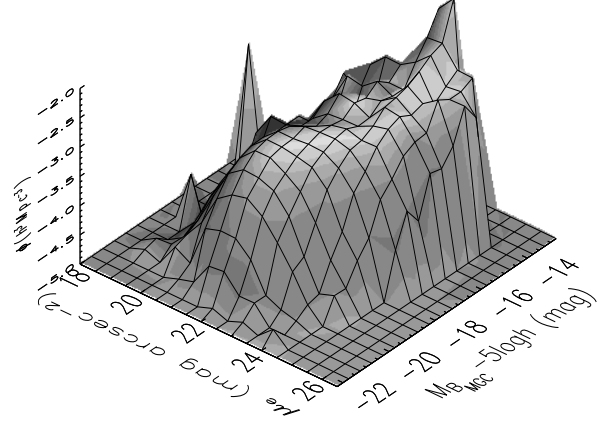


**Figure 11.** The normalised bivariate brightness distribution. The vertical axis is logarithmic in units of  $h^3 \text{ Mpc}^{-3} \text{ mag}^{-1} (\text{mag arcsec}^{-2})^{-1}$ .

Davies & Disney 1990), although not precisely as it does not account for the variation of physical cross-section with redshift or for isophotal corrections. The steep sides of the  $\sum_i H_{ijk}$  surface (Fig. 8) highlights the narrow range over which surface brightness selection effects go from negligible to extreme and hence the importance of understanding a survey's selection limits.

#### 4 THE MGC BIVARIATE BRIGHTNESS DISTRIBUTION

We now apply the above methodology to our MGC sample. To recap, we extract galaxies in the range  $13 < B_{\text{MGC}} < 20$  mag, determine individual  $K$ -corrections, determine seeing-corrected surface brightness estimates, attach an incompleteness weight to each galaxy, reject galaxies which lie outside of their designated reliably observable regions (7 galaxies too large, 99 too compact and 22 too dim), generate weighting and visibility matrices for each galaxy and then iteratively apply equation (5) until a stable set of  $\phi(M, \mu^e)$ -values is found. Fig. 11 shows the result of this procedure after renormalisation (described below). It is worth noting that the majority of the rejected galaxies are extremely compact and have entered our sample only through spectroscopy of apparently stellar objects (2QZ, SDSS QSO survey, NED and MGCz).

The SWML method, by its construction, loses all information regarding the absolute normalisation (cf. Efstathiou et al. 1988). Here the normalisation issues are compounded by the consideration of selection bias. We overcome this by calculating the number of galaxies in the absolute magnitude and absolute surface brightness interval  $-20 < M_B - 5 \log h < -19.5$  mag and  $20 < \mu^e < 24$  mag arcsec<sup>-2</sup>. This parameter space is observable for any  $K(z)$  over the redshift range,  $0.047 < z < 0.162$  (equivalent to a co-moving volume of  $311\,849 h^{-3} \text{ Mpc}^3$  for the  $30.883 \text{ deg}^2$  field-of-view). Within these redshift, absolute magnitude and surface brightness ranges there are 785 galaxies with a summed weight, due to incompleteness, of 787.8. The  $\phi$  values are now rescaled to reproduce the correct space density for these galaxies (i.e.,  $0.00253 \pm 0.00020 h^3 \text{ Mpc}^{-3}$ ). The error in-

cludes both Poisson and large scale structure considerations and was derived from mock 2dF NGP catalogues (Cole et al 1998; <http://star-www.dur.ac.uk/~cole/mocks/main.html>) extracted from the Virgo Consortium Hubble Volume. Volumes equivalent in shape to the MGC normalisation volume were extracted and the standard deviation of  $-20 < M_B - 5 \log h < -19.5$  mag galaxies determined. The final error, inclusive of large scale structure, is roughly twice that of the Poisson error alone.

Fig. 12 shows the final normalised BBD on a logarithmic scale. The thick dotted line shows the region within which the statistical errors are 25 per cent or less. The thick solid line shows the effective detection limit defined as the BBD region sampled by at least 100 galaxies (equivalent to a volume limit of  $\sim 1800 h^{-3} \text{ Mpc}^3$ ). The detection limit bounds the BBD at the low surface brightness and faint limits and clearly starts to impinge on the distribution from around  $M_B - 5 \log h \approx -18$  mag (coincidentally the usually adopted boundary between the dwarf and giant galaxy populations). This confirms that even the MGC, the deepest local imaging survey to date, remains incomplete for both high ( $M_B - 5 \log h \approx -15$  mag) and low surface brightness galaxies. To sample these regions requires both deeper ( $\mu_{\text{LIM}}^e \gg 26 \text{ mag arcsec}^{-2}$ ) and higher resolution imaging data ( $\Gamma \ll 1.27 \text{ arcsec}$ ) over a comparable or larger area ( $\Omega \geq 30 \text{ deg}^2$ ) with high spectroscopic completeness.

Following de Jong & Lacey (2000) and Cross & Driver (2002) we attempted to fit the MGC BBD with a Choloniewski function (Choloniewski 1985), given by:

$$\phi(M, \mu^e) = \frac{0.4 \ln 10}{\sqrt{2\pi} \sigma_{\mu^e}} \phi^* 10^{0.4(M^* - M)(\alpha + 1)} e^{-10^{0.4(M^* - M)}} \times \exp \left\{ -\frac{1}{2} \left[ \frac{\mu^e - \mu^{e*} - \beta(M - M^*)}{\sigma_{\mu^e}} \right]^2 \right\} \quad (8)$$

The parameters  $\phi^*$ ,  $M^*$  and  $\alpha$  are the conventional Schechter function parameters (Schechter 1976). The three additional parameters,  $\mu^{e*}$ ,  $\sigma_{\mu^e}$  and  $\beta$  are the characteristic surface brightness, the Gaussian width of the surface brightness distribution and the luminosity-surface brightness relation respectively. This function has been derived analytically by Dalcanton et al. (1997), Mo et al. (1998) and de Jong & Lacey (2000). Note that the additional normalisation factor,  $(\sqrt{2\pi} \sigma_{\mu^e})^{-1}$ , ensures that  $\phi^*$ ,  $M^*$  and  $\alpha$  are directly equivalent to the more familiar Schechter function parameters. The fit is achieved using the downward simplex method (Press et al. 1992) and the 1- $\sigma$  errors are derived from a one-dimensional  $\chi^2$ -minimisation across each parameter ( $1\sigma \equiv \Delta\chi^2 = 158.9$ ).

For the 151 degrees of freedom (157 data values minus 6 model parameters) we find an unreduced  $\chi^2_{\text{min}}$  of 608.7. This suggests that the Choloniewski function is a poor fit to the data (see Fig. 13). The main reason appears to be the intrinsic assumption of a constant  $\sigma_{\mu^e}$ , whereas the distribution shown in Fig. 11 clearly broadens, a feature also observed by Shen et al. (2003) in their SDSS data. We discuss this further in Section 4.2. Choloniewski parameters and associated errors are tabulated in the upper half of Table 2 along with other published data including our previous measurement based on the 2dFGRS (Cross & Driver 2002).

#### 4.1 The space density of galaxies

Of particular interest over the past few decades has been the galaxy luminosity distribution. This can be derived from the BBD by integrating over the surface brightness axis, (the associated errors are the root sum squares of the individual errors for each bin). Fig. 14

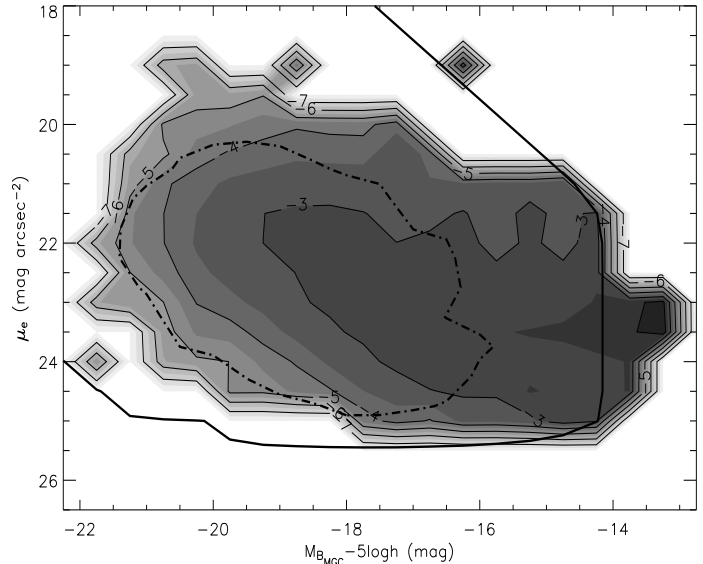


**Figure 12.** The final space density or bivariate brightness distribution of galaxies shown as both a greyscale image and contours on logarithmic scales in units of  $h^3 \text{ Mpc}^{-3} \text{ mag}^{-1} (\text{mag arcsec}^{-2})^{-1}$ . The contour spacing is 1 dex in  $\phi$  with the greyscale at 0.5 dex intervals. The thick solid line denotes the selection boundary defined as the BBD region where at least 100 galaxies could have been detected and is equivalent to an effective volume limit of  $1800 h^{-3} \text{ Mpc}^3$ . The thick dashed line encompasses the region within which the statistical error is smaller than 25 per cent.

(left panel) shows the result:  $\phi^* = (0.0177 \pm 0.0015) h^3 \text{ Mpc}^{-3}$ ,  $M_B^* - 5 \log h = (-19.60 \pm 0.04) \text{ mag}$  and  $\alpha = -1.13 \pm 0.02$ . Note that the error in the normalisation parameter,  $\phi^*$ , is the combination (in quadrature) of the error from the fitting algorithm combined with the error from the number of galaxies within the normalisation volume. For completeness we also show the implied LF from our Choloniewski function fit (dotted line). However recall the poor  $\chi^2_{\text{min}}$  value from this fit which highlighted the fit's inability to model the dwarf population correctly (mainly due to the broadening of the surface brightness distribution). The right panel of Fig. 14 shows the formal 1,2,3- $\sigma$  error contours for the Schechter function fit to the collapsed MGC BBD luminosity distribution.

##### 4.1.1 Comparison to the ESP, 2dFGRS and SDSS LFs

Fig. 15 compares our LF based on the BBD analysis of the deeper, higher quality, higher completeness MGC data to a number of other recent LF estimates (tabulated in the lower half of Table 2). Note that these Schechter functions are shown with their original  $\phi^*$ -values as opposed to the Liske et al. (2003) corrected values. We find our LF recovers a comparable  $M^*$  value to most previous surveys, but a slightly higher normalisation (as one might expect from a BBD-style analysis which recovers more light from the low surface brightness population than a non-BBD style analysis), and an  $\alpha$  value consistent with the median of these other surveys. In comparison to the ESP LF (Zucca et al. 1997) we find consistent Schechter function parameters within the quoted errors of the two surveys. In comparison to the 2dFGRS LF (Norberg et al. 2002) we find consistent  $M^*$  and  $\phi^*$  values but a flatter (more positive)  $\alpha$ . This discrepancy in  $\alpha$  is formally significant at the 3 $\sigma$ -level, however we do note that the 2dFGRS has undergone a major overhaul

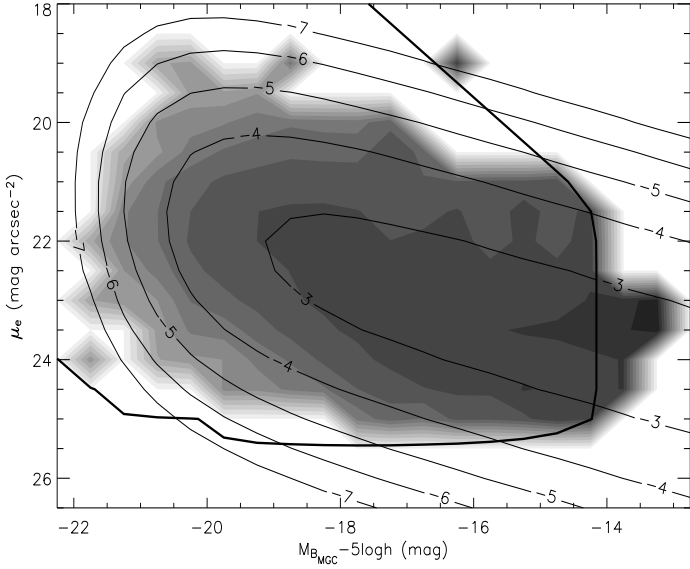


**Figure 13.** The contours show the Chółoniewski function which best fits our final BBD in units of  $h^3 \text{ Mpc}^{-3} \text{ mag}^{-1} (\text{mag arcsec}^{-2})^{-1}$ . The greyscale image and the thick solid line are the same as those in Fig. 12.

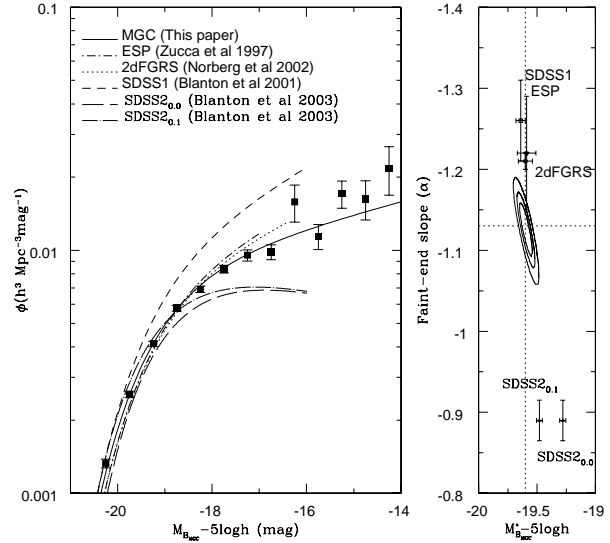


**Figure 15.** A comparison of recent luminosity function estimates as indicated (left panel) and the associated errors in  $M^*$  and  $\alpha$  together with the MGC 1, 2 and 3- $\sigma$  contours (right panel).

4.1.2 *Exploring the discrepancy with the SDSS LFs*

The most noticeable outliers in Fig. 15 are the two SDSS results, SDSS1 (Blanton et al. 2001) and SDSS2 (Blanton et al. 2003a). The discrepancy in the normalisation of SDSS1 has been comprehensively discussed by both Norberg et al. (2002) and Blanton et al. (2003a) and ascribed to the lack of an evolutionary model in the SDSS1 analysis, coupled with their method of normalisation. An over-density in the SDSS commissioning data region also contributes. The SDSS1 normalisation has been revised by Liske et al. (2003):  $\phi_{\text{SDSS1}}^*(\text{NEW}) = 0.76 \phi_{\text{SDSS1}}^*(\text{OLD})$ . Once corrected, the SDSS1 LF agrees well with the MGC ( $2\sigma$ -discrepancy in  $\alpha$ ), the 2dFGRS and the ESO Slice Project (ESP) estimates.

The more recent SDSS2 result has a significantly fainter  $M^{*2}$  and a much flatter faint-end slope than any of the other surveys. Blanton et al. (2003a) argued that the difference in the  $r$ -band LFs of SDSS1 and SDSS2 was simply due to the inclusion of luminosity evolution in the latter and that the luminosity densities measured by the 2dFGRS and SDSS2 agreed to within the errors once the differing amounts of evolution had been taken into account. However, in the  $g$ -band the discrepancy in  $\alpha$  between SDSS1 and SDSS2 is more than twice that in the  $r$ -band. Furthermore, even though the luminosity evolution derived in the SDSS2 fitting process is very strong ( $Q = 2.04$  mag per unit redshift, where  $M^*(z) = M^*(z=0) - Qz$ ) it cannot explain away the difference between the MGC and SDSS2 values. Our evolutionary correction given in Section 3.3 corresponds to  $Q \approx 0.74$ . If we replace this with the SDSS2 evolution,  $E(z) = -2.04z$ , and re-derive our collapsed MGC LF we find  $M_B^* - 5 \log h = -19.36$  mag and  $\alpha = -1.08$  (or  $M_B^* - 5 \log h = -19.36$  mag and  $\alpha = -1.06$  if we restrict the LF fitting to the equivalent SDSS2 limit of  $M_B - 5 \log h < -16$  mag). Hence some tension remains between the SDSS2 and MGC

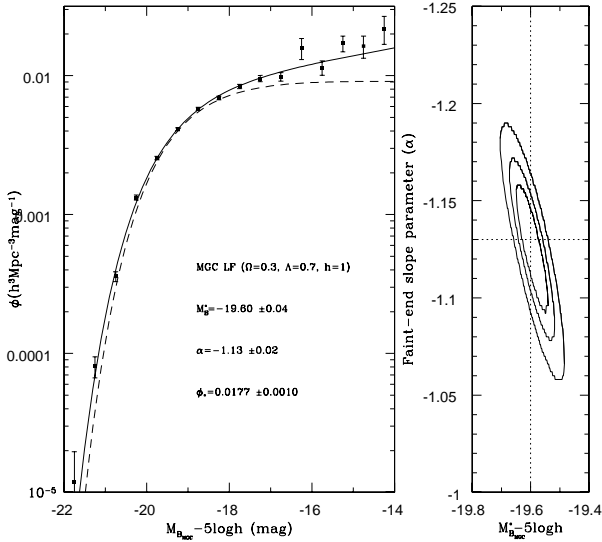


**Figure 14.** Left panel: the luminosity function derived by integrating the BBD over surface brightness with the best-fit Schechter function (solid line). Also shown is the implied Schechter function from the fitted Chółoniewski function (dashed line). Right panel: the 1, 2 and 3- $\sigma$  contours of the Schechter function fit.

of its photometry since this result (see discussion in Cross et al. 2004). The final 2dFGRS post-recalibration LF has yet to be determined. Our result are consistent with the  $M^*$  value only for SDSS1 and inconsistent with all three Schechter function values for SDSS2. A detailed discussion of this discrepancy follows in the next section.

<sup>2</sup> Note that the conversion from  $^{0.1}g$  to  $B_{\text{MGC}}$  is given by Blanton et al. (2003a) as  $B_{\text{MGC}} = ^{0.1}g - 0.09$ .

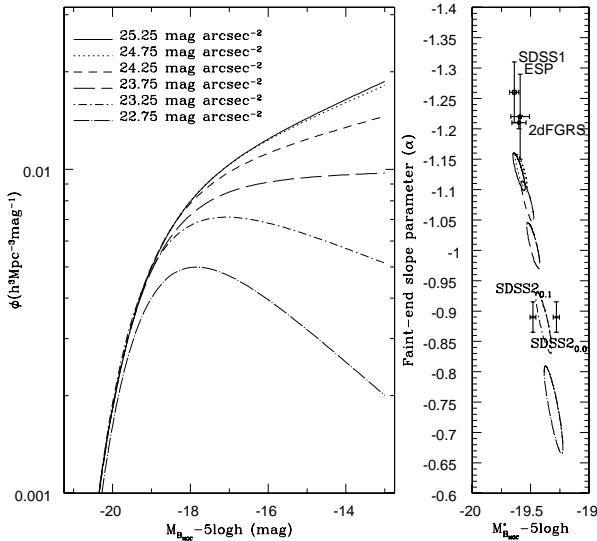


**Figure 16.** The left panel shows the result of a re-analysis of the MGC data with various low surface brightness selection limits imposed (as indicated). This figure demonstrates the extreme sensitivity of the recovered Schechter function parameters to the spectroscopic surface brightness completeness limit. The right panel shows  $1\text{-}\sigma$  error ellipses for the Schechter function fits along with the data points from the right panel of Fig. 15.

LFs irrespective of evolution. The same argument holds when comparing SDSS2 to the 2dFGRS since the latter adopted an evolution equivalent to  $Q \approx 1.15$ .

To test whether the surface brightness selection limits might be responsible, Fig. 16 shows a re-analysis of the MGC data, following the same procedures as before, but now imposing progressively shallower surface brightness limits (as indicated). The left panel again shows the LFs and the right panel the  $1\text{-}\sigma$  error ellipses of the Schechter function fits. It is quite apparent that shallower surveys progressively miss a greater fraction of the dwarf population(s) – and ultimately giants – recovering both a fainter  $M^*$  and a more positive  $\alpha$ . In fact, Fig. 16 based on MGC data mirrors the expectation from the simulations of Cross & Driver (2002) remarkably well (see their Fig. 5).

On Fig. 16 with an imposed selection limit of  $23.25 \text{ mag arcsec}^{-2}$  appears to match the SDSS2 LF closely and initially suggests that surface brightness selection might explain the SDSS2 result. (Note that SDSS1 implemented a BBD-style analysis). However Fig. 3 (left panels) do not show a significant difference in the low surface brightness spectroscopic completeness between the 2dFGRS and SDSS surveys suggesting limits closer to  $24.25 \text{ mag arcsec}^{-2}$ . We note that the SDSS2 surface brightness 50 per cent completeness limit (including consideration of deblending and flux loss issues, etc.) is quoted as  $\mu_r^e[\text{Circular}] \approx 23.4 \text{ mag arcsec}^{-2}$  (Blanton et al. 2005a, their fig. 3), where [Circular] indicates that the SDSS surface brightness measures are derived from ‘circular’<sup>3</sup> half-light radii. Conversely

the MGC (and most contemporary datasets) use major axis half-light radii. These are derived by growing the optimal ellipse until it encloses 50 per cent of the flux. The use of a circular aperture will always result in a lower half-light radius than an elliptical aperture (except for purely face-on systems), and hence in a higher effective surface brightness. The two effective surface brightnesses are related by:

$$\mu^e[\text{MajorAxis}] = \mu^e[\text{Circular}] - 2.5 \log \left( \frac{b}{a} \right), \quad (9)$$

where  $(b/a)$  is the axis ratio. For a random distribution of infinitely thin disks the expected median axis ratio  $\langle b/a \rangle$  is 0.5. In reality the galaxy distribution is more diverse consisting of spheroids, bulges and thick disk components/systems. Circular half-light radii measurements are also somewhat resolution dependent, introducing both seeing and redshift dependencies into the conversion. Empirically we find for our MGC data:  $\langle b/a \rangle_{\text{MGC}} = 0.71$ , implying a correction of  $0.37 \text{ mag arcsec}^{-2}$ . Although we cannot directly compare our MGC elliptical half-light radii to the circular Sérsic half-light radii used by SDSS2, we can compare them to the standard SDSS-DR1 circular Petrosian half-light radii. We find  $\langle r_{50, \text{Petrosian}}/r_{\text{MGC}} \rangle = 0.84$ , independently confirming the correction of  $0.37 \text{ mag arcsec}^{-2}$ . Hence the quoted SDSS2 50 per cent completeness limit of  $\mu_r^e[\text{Circular}] = 23.4 \text{ mag arcsec}^{-2}$  equates to  $\mu_r^e[\text{MajorAxis}] = 23.77 \text{ mag arcsec}^{-2}$ .

The colour correction is more complex as it depends strongly on galaxy type and luminosity. The low luminosity population is the bluest ( $\langle B_{\text{MGC}} - r \rangle \approx 0.5 \text{ mag}$ ) and hence surface brightness incompleteness will preferentially affect the faint end of the LF. Evidence for such a colour completeness bias can be seen in the observed SDSS incompleteness within the MGC region. This is shown as a function of  $(g - r)$  or  $(u - r)$  versus  $\mu_{\text{app}}^e$  in the middle row (centre and right panels) of Fig. 3. As the SDSS spectroscopic survey is  $r$ -band selected it should not be surprising that the  $B_{\text{MGC}}$  completeness is a more complex surface in magnitude, surface brightness and colour. In the worst case scenario we find a 50 per cent completeness limit for the bluest systems of  $\mu_{B_{\text{MGC}}}^e = 24.27 \text{ mag arcsec}^{-2}$  which is consistent with Fig. 3 (middle left), but more importantly significantly fainter than the surface brightness limit implied by Fig. 16. That a colour selection is obvious in both the  $(g - r)$  and  $(u - r)$  SDSS completeness maps of Fig. 3 argues that the colour selection bias is not a feature of the  $u$  band data but more a general trend across all filters.

Adopting an appropriate  $\mu_{B_{\text{MGC}}}^e$  selection criterion is clearly non-trivial, however a simple way forward is to construct a LF from the available SDSS2 redshifts within the MGC region (see Table. 1). This will have the SDSS selection function inherently built in. We adopt  $m_{\text{faint}} = 18.5 \text{ mag}$ ,  $\mu_{\text{lim}}^e = 24.27 \text{ mag arcsec}^{-2}$ , the SDSS2  $g$ -band evolutionary correction and apply a conventional univariate step-wise maximum likelihood (Efstathiou et al. 1988). We now recover  $M_B^* = (-19.26 \pm 0.07) \text{ mag}$  and  $\alpha = -0.83 \pm 0.06$  (or  $M_B^* = (-19.26 \pm 0.07) \text{ mag}$  and  $\alpha = -0.82 \pm 0.06$  for  $M_B < -16 \text{ mag}$ ) and consistent at the  $\sim 1\text{-}\sigma$  level with SDSS2. We therefore conclude that the discrepancy between the MGC and SDSS2 LFs is complex, but predom-

radii for moderate and highly inclined systems, particularly given the additional dependencies this will introduce as a function of both seeing and distance. It is also not clear why Blanton et al. (2003a) prefer Sérsic fitted half-light radii rather than their more reliable (Blanton et al. 2005b) empirically measured Petrosian radii (which agree closely with MGC circularised half-light radii).

<sup>3</sup> The SDSS2 surface brightness measure is derived from the combination of SDSS Petrosian magnitudes and Sérsic half-light radii based on circular aperture photometry. At this point it is not clear why the SDSS team have adopted circular apertures and how one should interpret circular half-light

inantly due to the colour bias within the SDSS (cf. Fig. 3 middle right). This highlights the additional complexity in measuring LFs for filters other than the spectroscopic selection filter.

#### 4.1.3 Lower limits on the very faint-end

Finally we note the recent preprint by Blanton et al. (2005a) in which an attempt is made to sample the very low luminosity regime from their New York University Value Added Catalogue (Blanton et al. 2005b). This incorporates a strategy for correcting the surface brightness incompleteness within the SDSS2 dataset resulting in a significantly steeper faint-end slope ( $\alpha = -1.28$  to  $-1.52$  in  $r$ ). The premise is that the surface brightness distribution of the dwarf population can be extrapolated from that of the giant population. This results in correction factors for the space density of dwarf systems of up to 3.5 (see Blanton et al. 2005a, their fig. 6). In a similar spirit of producing a ‘best guess’ LF at low luminosities Fig. 17 shows the MGC LF with the selection boundaries and lower redshift bounds removed. This undoubtedly represents an underestimate of the true space density at low luminosities ( $M_B - 5 \log h > -14$  mag), but in so far as a comparison can be made it is consistent with the SDSS result (Blanton et al. 2005a), in the sense that the SDSS data lie above the MGC lower limits. Our LF is also consistent with a compilation of 231 galaxies within the local sphere ( $D < 5$  Mpc) taken from Karachentsev et al. (2004). Apart from indicating the amount of work that is yet to be done, Fig. 17 does suggest that the low redshift global luminosity function must steepen beyond  $\alpha = -1.13$  at some intermediate magnitude ( $M_B - 5 \log h > -16$  mag). However it would seem unlikely that it could steepen enough for the dwarf systems to make a significant contribution to the total local luminosity density (as indicated by the dashed line).

## 4.2 The surface brightness distribution

As we found earlier the Choloniewski function adopted by previous studies (de Jong & Lacey 2000; Cross & Driver 2002) provides a poor fit to the joint luminosity-surface brightness distribution. This is mainly due to the apparent broadening of the surface brightness distribution towards fainter luminosities. Fig. 18 highlights this by showing the surface brightness distribution at progressively fainter absolute magnitude intervals along with the selection limits taken from Fig. 12. We attempt to fit each of these distributions (Fig. 18, solid lines) with a Gaussian function defined as:

$$\phi(\mu^e) = \frac{\phi^*}{\sqrt{2\pi}\sigma_{\mu^e}} \exp \left[ -\frac{1}{2} \left( \frac{\mu^{e*} - \mu^e}{\sigma_{\mu^e}} \right)^2 \right], \quad (10)$$

where,  $\mu^{e*}$  is the characteristic (peak) surface brightness and  $\sigma_{\mu^e}$  is the dispersion (analogous to those values in the Choloniewski function). The errors reflect  $\sqrt{n}$ -statistics from the original observed number of galaxies contributing to each histogram element. For elements with zero values (i.e., no galaxies detected) we adopt the error appropriate for a detection of one galaxy so that the significance of these ‘null’ detections can be used to help constrain the fits. The number of degrees of freedom (listed in the final column of Table 3) is the number of data values plus any zero values either side of the distribution within the selection boundaries minus the number of fitting parameters (three). Fig. 19(a) shows the  $\mu^{e*}$  (dark grey line) and  $1-\sigma_{\mu^e}$  values (shaded region) as a function of absolute magnitude. These results are also tabulated in Table 3. Fig. 19(a) shows

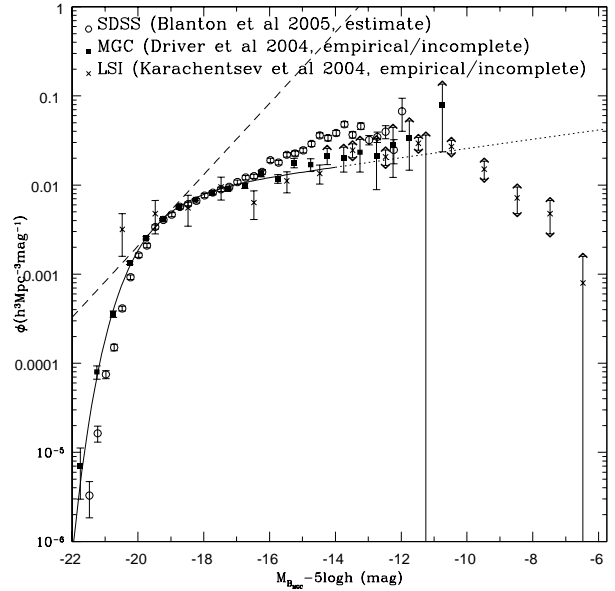


**Figure 17.** Tentative constraints on the very faint end of the galaxy luminosity function from three independent studies. Solid squares: available MGC data using the BBD-style analysis but with all limits removed. These data are incomplete at the faint end with the loss of both high and low surface brightness systems and therefore represent lower limits only. Open circles: a recent ‘speculative’ SDSS estimate (Blanton et al. 2005a) based on an extrapolation of the surface brightness distribution at bright magnitudes. Crosses: Local Sphere of Influence ( $D < 5$  Mpc) data taken from the catalogue of Karachentsev et al. (2004). The Schechter function from Fig. 15 is shown as the solid line and its extrapolation as the dotted line. The dashed line shows the contour of equal contribution to the overall luminosity density.

a trend of an initially invariant luminosity-surface brightness relation until  $M_B - 5 \log h \approx -19$  mag, and then a steady decline to the limits of detection at  $M_B - 5 \log h \approx -14$  mag. The dispersion of the surface brightness distributions grows steadily broader as the luminosity decreases. The changes in both the luminosity-surface brightness relation and its dispersion explain the poor fit of the Choloniewski function which cannot accommodate such features.

At this stage it is also worth noting that the Gaussian fits return poor  $\chi^2_{\min}$  values at intermediate luminosities with even a hint of bimodality (at  $M_B - 5 \log h \approx -16$  mag). This may imply that the low luminosity distribution consists of two overlapping populations: rotationally supported disks (lower surface brightnesses) and pressure supported spheroids (higher surface brightnesses). If borne out by more detailed structural studies then one might expect the rotationally supported disk systems to exhibit both a steeper  $M-\mu$  relation and a narrower surface brightness distribution than the overall population.

#### 4.2.1 Comparison to established structural trends

Three luminosity-surface brightness trends ( $L-\Sigma$ ) are well known (see Table 2): the Kormendy relation for spheroids (Kormendy 1977); Freeman’s Law for disks (Freeman 1970); and the Virgo/Local Group dwarf relation (Impey, Bothun & Malin 1988; Mateo 1998). More recently de Jong & Lacey (2000) identified a relation for late-type disks similar to that seen for dwarf systems

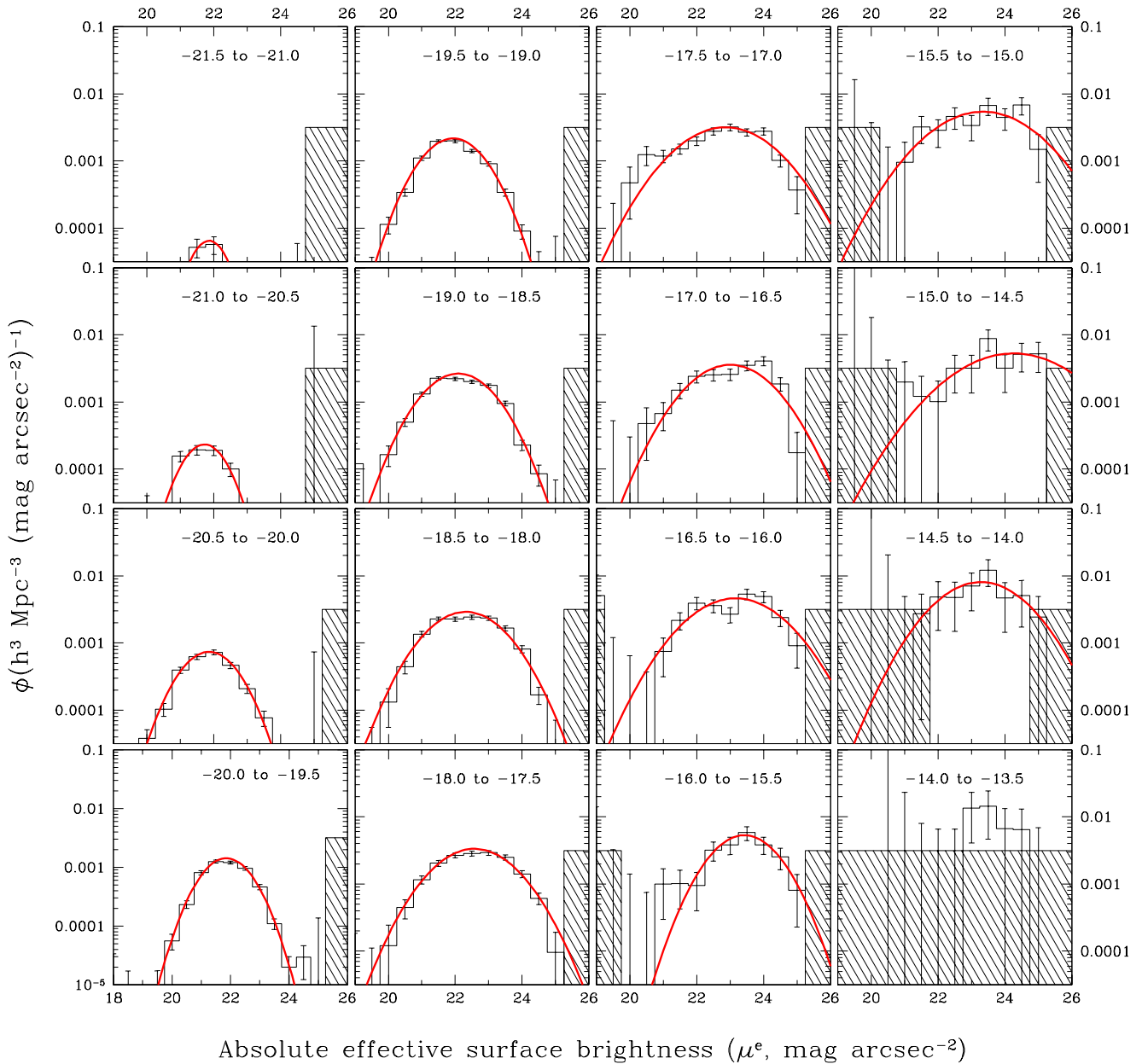


**Figure 18.** Slices of the BBD along the surface brightness axis in intervals of constant luminosity as indicated (histogram with errorbars). Note that the data within shaded regions are not used in the determination of the Gaussian fits (shown as solid lines).

in Virgo and the Local Group. The general trends for these established relations are overlain on Fig. 19(a). One can speculate that the combination of these trends might well lead to the overall shape of the global  $L$ - $\Sigma$ -distribution shown on Fig. 19(a), as the spheroid-to-disk ratio typically declines with decreasing luminosity. Hence the global trend initially follows a Kormendy relation, switching to a more constant Freeman Law and finally into a declining dwarf relation. In comparison to the de Jong & Lacey (2000) sample for late-type disks we find a shallower luminosity-surface brightness relation and a broader surface brightness distribution. This may have two reasons: firstly, the dJL sample is  $I$ -band selected and

our use of a global filter conversion may introduce this error; secondly, the dJL sample is far more local and both inclination and dust-corrected. An obvious extension to the MGC analysis would be to also implement these corrections.

Obviously, detailed structural analysis is required before a meaningful comparison to these ad hoc local studies can be made. However, we can highlight two key questions: (i) Are there two distinct disk populations, i.e. a giant disk population adhering to Freeman's Law and a dwarf-disk population which does not, or just a single dwarf-disk relation? (ii) Is the dwarf surface brightness

distribution bimodal reflecting the two dominant classes of dwarf galaxies (dwarf ellipticals and dwarf irregulars)?

#### 4.2.2 Comparison to previous global $L$ - $\Sigma$ studies

There are three significant studies of the global  $L$ - $\Sigma$  distribution (see Table 2): a 2dFGRS study by Cross et al. (2001), an SDSS study by Shen et al. (2003) and a local galaxy SDSS study by Blanton et al. (2005a).

In comparison to Cross et al. (2001) we find that the MGC data follow a similar  $L$ - $\Sigma$  relation but show significantly broader surface brightness distributions. Fig. 19(b) shows the comparison where we have taken the data from Table C2 of Cross et al. (2001) and fitted Gaussian distributions in a similar manner as for the MGC data. The obvious discrepancy is in the  $\sigma_{\mu^e}$  values and this reflects a number of significant improvements. Firstly, the deeper MGC isophote coupled with the improved redshift completeness of MGCz (see Fig. 3) enables the inclusion of lower surface brightness systems. As these preferentially occur at lower luminosity the effect acts to broaden the surface brightness distribution at fainter luminosities. Secondly, the 2dFGRS sample was not seeing-corrected and hence the sizes of the high surface brightness galaxies were overestimated. Thirdly, the Cross et al. analysis derived the surface brightness measurements under the assumption that all galaxies were perfect exponential disks. These factors conspire to push the 2dFGRS BBD into a narrower distribution. A fourth factor, hard to qualitatively assess, is the major revisions to the 2dFGRS photometry which have taken place since Cross et al. (2001) (see Cross et al. 2004 for further details on the 2dFGRS recalibration history).

In Fig. 19(c) we overlay the recent SDSS results by Shen et al. (2003). The Shen et al. study is  $r_{0.1}$ -band selected with an imposed surface brightness cut at  $\mu_r^e[\text{Circular}] = 23 \text{ mag arcsec}^{-2}$ . Shen et al. divide their sample into a number of sub-groupings and we elect to show the data from their Fig. 13 which separates galaxies according to concentration index,  $c$  (see Nakamura et al. 2003 for details). This divides the population into galaxies earlier or later than S0/a (with an 83 per cent success rate). To convert the Shen et al.  $r$ -band results to  $B_{\text{MGC}}$  we derive the early and late-type ( $B_{\text{MGC}} - r$ ) colour in each of the  $r$ -band absolute magnitude bins specified by Shen et al. To do this we assume our eyeball E/S0 type corresponds to ‘early’ and our eyeball Sabcd/Irr to ‘late’ (a detailed account of the eyeball morphologies and morphological luminosity functions is presented in Driver et al., in preparation). Hence each data point is adjusted independently. In addition we must also correct the SDSS effective surface brightness measurements from circular to major axis measurements as discussed in Section 4.1.2, i.e.  $\mu^e[\text{MajorAxis}] = \mu^e[\text{Circular}] + 0.37$ . Fig. 19(c) shows the comparison between the Shen et al. data and the MGC and we see a uniform offset of  $\delta\mu^e \approx 0.4 \text{ mag arcsec}^{-2}$ . Despite extensive experimentation with various data subsets and selection boundaries we have been unable to reproduce this result from the MGC data.

Fig. 19(d) shows a comparison between the recent very low redshift SDSS  $r$  results (Blanton et al. 2005a) and the MGC. We implement the same colour and surface brightness corrections as for the Shen et al. data. The ridge line of the very local SDSS data shows good agreement with the MGC data, albeit with a narrower distribution (i.e., lower  $\sigma$  values). However this appears to be a further manifestation of the SDSS use of circular apertures. For example, if we derive the surface brightness distribution around the  $M^*$ -point for the MGC data using circular and major axis derived surface brightness measures we find a peak offset of  $0.42 \pm 0.03$  (slightly larger than our estimated median offset of

0.37) with  $\sigma_{\text{MajorAxis}} = 0.74 \pm 0.02$  and  $\sigma_{\text{Circular}} = 0.60 \pm 0.02$ . This latter value is now consistent with the recent SDSS estimate (Blanton et al. 2005a). Note that the dashed lines on Fig. 19 indicated the SDSS extrapolated data used to correct the faint-end of the luminosity function. To the MGC limit these extrapolated distributions appear to match our data well providing some vindication for the extrapolation process (see Blanton et al. 2005a, Section 4.1.3 and Fig. 17).

The above two comparison between the MGC and the Shen et al. (2003) and Blanton et al. (2005a) studies must imply an inconsistency between the two SDSS results. This is perhaps more obvious if one bypasses the MGC data and directly compare Fig. 14 of Shen et al with Fig. 5 of Blanton et al. The peaks of the late-type/low seric index SB distributions (both measured in  $r$ ) are clearly distinct. Given the consistency with the 2dFGRS and the traditional structural studies discussed earlier we conclude that the problem most likely lies with the Shen et al. analysis. If we disregard the Shen et al study, we can conclude that the ridge line of the effective surface brightness distribution is well constrained and consistent between the MGC, 2dFGRS and the most recent SDSS results. However the MGC distribution is significantly broader than either the 2dFGRS or SDSS results which is due to improvements in the analysis (in comparison to the 2dFGRS) and the use of elliptical as opposed to circular aperture photometry (in comparison to the SDSS).

### 4.3 Constraining the evolution of $M^*$ galaxies

In Section 3.3 we described our adopted evolutionary parameter,  $\beta$ , where the luminosity evolution follows the form:  $E(z) = 2.5 \log[(1+z)^{-\beta}]$ . In Section 4.1.2 we saw that this evolution differs from that adopted by the 2dFGRS and SDSS2 and discussed the possible impact. Fig. 20 (upper panels) highlights this dependency by showing the derived values for  $M^*$  and  $\alpha$  for various values of  $\beta$ . Taking this one step further we can attempt to constrain  $\beta$  directly by adopting the additional constraint that the recovered  $M^*$  parameter should be invariant to redshift. We divide our sample into two redshift intervals:  $0.013 < z < 0.1$  and  $0.1 < z < 0.18$  (with median redshifts of 0.08 and 0.13 respectively) and redetermine the collapsed LF distributions using our BBD analysis for regular intervals of  $\beta$ . We hold  $\alpha$  fixed to the value derived from the full redshift range for each  $\beta$  (i.e., the value indicated in the middle panel of Fig. 20) and solve for  $M^*$  and  $\phi^*$ . It is necessary to hold  $\alpha$  fixed because the high- $z$  sample has too few low-luminosity galaxies to adequately constrain it. Fig. 20 (main panel) shows the resulting  $\Delta M^*$  versus  $\beta$  and we find the weak constraint:  $-2.0 < \beta < 1.25$ . While this is not particularly stringent, it is consistent with our adopted value of  $\beta = 0.75$ . This constraint on beta is marginally inconsistent ( $2\sigma$ ) with the evolution found by Blanton et al. (2003a) for the  $g$ -band ( $\beta \approx 2$ ), but consistent with the evolution adopted by the 2dFGRS ( $\beta \approx 1$ ). Perhaps more importantly this range of  $\beta$  implies a potential systematic uncertainty on the quoted  $M^*$  ( $\alpha$ ) values of  $\pm 0.25 (\pm 0.04)$ . As noted at the start of Section 3, it is also equally plausible that this error does not actually reflect evolution per se but could instead be interpreted as a redshift dependent photometric error or similar.

## 5 CONCLUSIONS

In this paper we have attempted to recover the space density and surface brightness distributions of galaxies, paying careful atten-



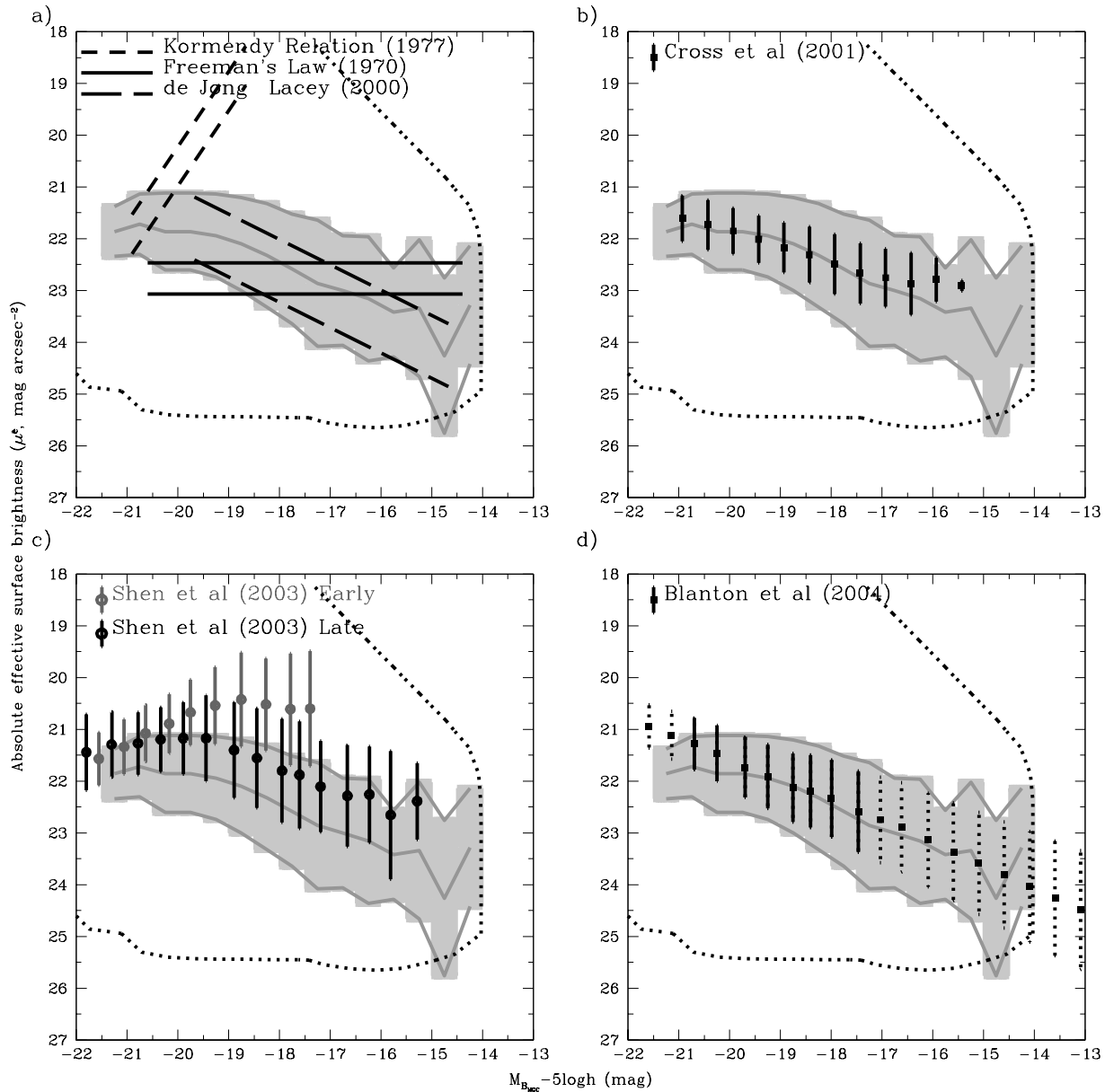


**Figure 19.** Four panels showing the  $1-\sigma_{\mu^e}$  ranges (grey shading) and the  $\mu^{e*}$  values (dark grey line) from the Gaussian fits of Fig. 18. On all panels the MGC selection boundary is shown by the outer dotted line and represents a volume limit of  $1800 h^{-3} \text{Mpc}^3$ , (see Fig. 12). (a) Overlain are the  $1-\sigma$  ranges for the canonical spheroid (Kormendy relation; short dashed line), disk (Freeman's Law; solid horizontal line) and late-type (de Jong & Lacey 2000; long dashed line) results. (b) A comparison to the  $b_J$ -band 2dFGRS results of Cross et al. (2001), data points and  $1-\sigma$  ranges. (c) A comparison to the  $r$ -band SDSS results of Shen et al. (2003). Details of the colour correction are given in the text. Shen et al. divide their sample by concentration index into 'early' ( $c > 2.86$ , black symbols) and 'late' types ( $c < 2.86$ , grey symbols). At most magnitudes the late-types dominate the space density and so the most meaningful comparison, band-switch not withstanding, is between the MGC data points and the SDSS late types. (d) A comparison between the global SDSS2 distribution (Blanton et al. 2005a) transformed from  $r$  to  $B_{\text{MGC}}$  as for (c). The dashed symbols indicate the region of extrapolation.

tion to surface brightness selection biases. We have used the Millennium Galaxy Catalogue which, although smaller in size, has significantly higher resolution, greater depth and higher redshift completeness than either the 2dFGRS or SDSS datasets, hence probing to fainter intrinsic luminosities. In comparison to most earlier studies this work includes the following enhancements.

1. Imaging data which probes  $\sim 1-2 \text{ mag arcsec}^{-2}$  deeper than the 2dFGRS and SDSS surveys.
2. Exceptionally high spectroscopic completeness (96 per cent).
3. Individual  $K$ -corrections derived from  $uBgriz$  fits to spectral templates.

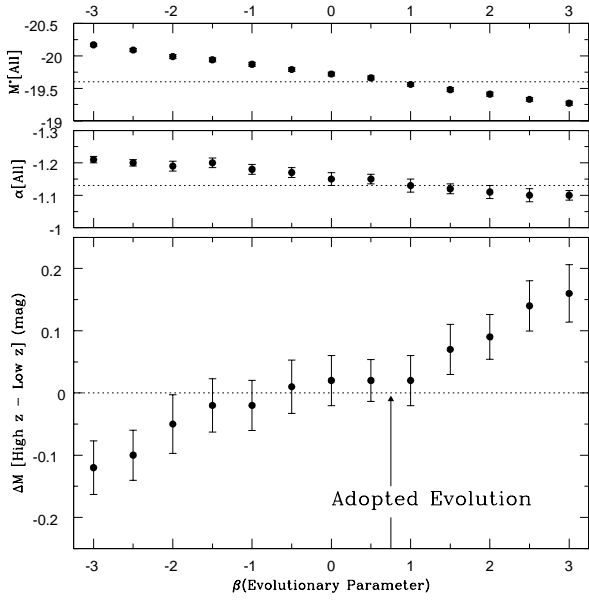


**Figure 20.** Main panel: constraining the evolutionary parameter  $\beta$  from the variation of  $M^*$  between low and high redshift samples. Upper panels: the  $M^*$  and  $\alpha$  values for the entire dataset for different beta values.

4. Seeing-corrected half-light radius measurements without assumption of profile shape.
5. Modeling of the MGC surface brightness detection and reliability limits which includes the effects of the analysis software.
6. A weighting system which accounts for apparent magnitude and apparent surface brightness dependent redshift incompleteness.
7. A joint luminosity-surface brightness step-wise maximum likelihood method which incorporates the selection boundaries.

### 5.1 The luminosity function

Having incorporated these additional improvements to the classical measurement of galaxy luminosity functions, we generally find close agreement with previous results. In particular, our collapsed luminosity distribution is marginally higher in normalisation and marginally flatter than the 2dFGRS (Norberg et al. 2002), ESP (Zucca et al. 1997) and SDSS1 (Blanton et al. 2001; after renormalisation by Liske et al. 2003) results. It is significantly brighter and steeper than the more recent SDSS2 luminosity function (Blanton et al. 2003a). We infer that this discrepancy arises because of a colour-selection bias in the SDSS. The MGC survey extends to lower luminosity than these previous surveys, providing more leverage and hence more reliability at the faint end. Our final Schechter function parameters are:  $\phi^* = (0.0177 \pm 0.0015) h^3 \text{ Mpc}^{-3}$ ,  $M_B^* - 5 \log h = (-19.60 \pm 0.04) \text{ mag}$  and  $\alpha = -1.13 \pm 0.02$  with a  $\chi^2/\nu$  of 19.6/15 indicating a respectable fit. Overall we find that surface brightness selection effects do not play a significant role at bright luminosities. However, the combination of the luminosity-surface brightness relation and the broadening of the surface brightness distribution is likely to lead to the loss of both low surface brightness and compact dwarf systems in contemporary surveys – hence the variation in  $\alpha$  (cf. Fig. 15 & 16 and discussion in Section 4.1). At the very faint end we provide lower limits which suggest that the luminosity function must turn up at some point faintwards of  $M_{B_{\text{MGC}}} - 5 \log h \approx -16 \text{ mag}$ .

### 5.2 The low redshift $b_J$ luminosity density

The final MGC Schechter function parameters, which include compensation for the effects of selection bias, imply a luminosity density of  $j_{b_J} = (1.99 \pm 0.17) \times 10^8 h L_\odot \text{ Mpc}^{-3}$  (adopting  $M_\odot = +5.3 \text{ mag}$  and  $B_{\text{MGC}} = b_J - 0.131$ , cf. Liske et al. 2003). This is fully consistent with the MGC revised values for the 2dFGRS, ESP and SDSS1 surveys (see Table 3 of Liske et al. 2003). It is also worth noting that this value is also consistent with the original 2dFGRS (Norberg et al. 2002) and ESP (Zucca et al. 1997) values. The more recent SDSS2 result (Blanton et al. 2003a) finds  $j_{b_J}^{z=0} = (1.54 \pm 0.10) \times 10^8 h L_\odot \text{ Mpc}^{-3}$  and  $j_{b_J}^{z=0.1} = (1.90 \pm 0.10) \times 10^8 h L_\odot \text{ Mpc}^{-3}$ . Hence while the  $z = 0.1$  value is consistent the  $z = 0$  value is not ( $3\sigma$ ). The SDSS  $z = 0$  value is derived by adopting the evolutionary parameters derived by Blanton et al. (2003a). If we use our evolution instead ( $\beta = 0.75$ , see Section 3.3) the SDSS  $z = 0$  luminosity density becomes  $j_{b_J}^{z=0} = (1.72 \pm 0.10) \times 10^8 h L_\odot \text{ Mpc}^{-3}$  which although closer is also inconsistent with our result. From Section 4.1.2 we concluded that a colour bias may have resulted in an underestimate of the SDSS  $g$ -band LF and hence to an underestimate of the SDSS luminosity densities.

Based on the consistency between the MGC, 2dFGRS and ESP results we can also find that while the more sophisticated BBD analysis does recover some additional flux from the low surface brightness population, it does not constitute a significant change (consistent with the findings of Driver 1999).

### 5.3 The joint luminosity-surface brightness relation

Our recovered bivariate brightness distribution exhibits a clear ‘ridge’ of data well separated from the selection boundaries down to  $M_B - 5 \log h \approx -16 \text{ mag}$  at which point both very compact and highly extended dwarf systems will be missed. This indicates that the recovered Schechter function is generally robust to surface brightness selection effects for luminous galaxies but that the dwarf population(s) remain elusive. We attempted to fit a Chołoniewski function (Chołoniewski 1985), essentially a Schechter function with a Gaussian distribution in surface brightness, to the overall distribution. It introduces three additional parameters: a characteristic surface brightness; a Gaussian dispersion; and a luminosity surface brightness relation. We find that this function fails to provide a satisfactory fit due to the broadening of the surface brightness distribution with decreasing luminosity and a distinct change in slope of the luminosity-surface brightness relation at  $M_B - 5 \log h \approx -19 \text{ mag}$ .

### 5.4 The surface brightness distribution(s)

We find that the surface brightness distribution of galaxies exhibits interesting behaviour, with a well bounded Gaussian-like distribution at  $L^*$ , qualitatively consistent with the combination of the Kormendy relation for spheroids and a  $2\times$  broader Freeman’s Law for bright disks. At  $L^*$  we find that the surface brightness distribution is well described by a Gaussian with parameters:  $\phi^* = (3.5 \pm 0.1) \times 10^{-2} h^3 \text{ Mpc}^{-3}$ ,  $\mu^{e*} = (21.90 \pm 0.01) \text{ mag arcsec}^{-2}$ ,  $\sigma_{\mu^e} = (0.77 \pm 0.02) \text{ mag arcsec}^{-2}$  with a  $\chi^2/\nu$  of 9.8/8. At fainter luminosities the normalisation increases, the characteristic surface brightness becomes fainter and the dispersion broadens until the distribution appears almost flat (or possibly bimodal). The Schechter function fit to the Gaussian normalisations (column 4 of

Table 3) provides a basic completeness correction and yields consistent Schechter function parameters to those quoted in Section 5.1, i.e.  $\phi^* = (0.0184 \pm 0.0008) h^3 \text{ Mpc}^{-3}$ ,  $M_B^* - 5 \log h = (-19.55 \pm 0.08) \text{ mag}$  and  $\alpha = -1.11 \pm 0.02$  with a  $\chi^2/\nu$  of 26.0/12.

In comparison to the 2dFGRS study of Cross et al. (2001) we find a consistent luminosity-surface brightness relation but with a significantly broader dispersion in surface brightness. This is predominantly due to the implementation of seeing corrected size, direct (i.e., profile-independent) half-light radius measurements and improved completeness for extended systems. A comparison to the SDSS results of Shen et al. (2003) and Blanton et al. (2005a) are complex because of the SDSS standard of circular aperture photometry. However we find that our results can be reconciled with those of Blanton et al. (2005a) but not with those of Shen et al. (2003). We also note that the SDSS use of circular apertures also leads to significantly narrower surface brightness distributions.

### 5.5 Confrontation with theory

Various studies (Fall & Efstathiou 1980; Dalcanton et al. 1997; Mo et al. 1998; de Jong & Lacey 2000; Bell et al. 2003) relate the Gaussian dispersion of the surface brightness distribution, or equivalently of the  $R_e^4$  distribution, to the dimensionless spin parameter of the dark matter halo,  $\lambda = J|E|^{1/2} G^{-1} M_{\text{halo}}^{-5/2}$  (Peebles 1969). The basic concept is that the baryons in the disk reflect the angular momentum state (rotational or dispersive) of the dark matter halo. While the luminosity relates to the mass, the disk scale-length relates to the specific angular momentum via the spin parameter. Numerical simulations generally predict values for  $\sigma_{\ln R_e} \approx 0.56 \pm 0.04$  (Bullock et al. 2001; see also Cole & Lacey 1996). This is most consistent with our observations at fainter luminosities. However, at brighter luminosities we find a significantly narrower dispersion  $\sigma_{\ln R_e} = 0.36 \pm 0.01$ . This may imply that brighter, more mature galaxies have evolved via mechanisms currently beyond the standard numerical simulations (i.e., the baryons have decoupled from the dark matter halo and evolved away from the halo properties). Alternatively it may argue for significant non-directional baryon infall onto the halo, muddying any coupling between the primordial baryons and the halo (Murali et al. 2002). Further possibilities might also include the presence of bulges in high luminosity systems whose properties depend more critically on a central supermassive black hole (Silk & Rees 1998).

One intriguing result of the simulations is the lack of variation of the surface brightness or size distribution with mass (Vitvitska et al. (2002)). However, the more detailed studies which actually follow individual halos *do* imply a greater variation in  $\lambda$  for low-mass systems. For example, Vitvitska et al. (2002) trace the history of three halos through the merging process. They clearly show that  $\lambda$  initially varies significantly as the halos grow but that it becomes more resilient to mergers once the halos reach sufficient mass. Ultimately all three halos converge towards a common value at high mass. This seems plausible as one would expect smaller systems to be more affected by mergers than more massive systems.

<sup>4</sup>  $R_e$  is the half-light radius measured in kpc. It is related to surface brightness by  $\mu^e = M + 2.5 \log(2\pi R_e^2) + 36.57$  and hence  $\sigma_{\mu^e} = 2.17\sigma_{\ln R_e}$ .

### 5.6 Summary

The surface brightness distribution of galaxies has been hotly debated for over thirty years since the advent of Freeman's Law and the conjecture that it is wholly a selection bias (Disney 1976). While in many minds the debate is resolved through deep HI studies (e.g. Zwaan et al. 1997) and Ly- $\alpha$  absorption line studies (Mo et al. 1998; Chen & Lanzetta. 2003), others remain loyal to Disney's conjecture (e.g. O'Neil, Andreon & Culliandre 2003) and still argue for a flat surface brightness distribution at all luminosities (Sprayberry et al. 1997; Dalcanton 1998; Dalcanton et al. 1997) implying a significant amount of hidden mass. At least in O'Neil et al.'s case this stance derives from neglecting the clear luminosity-surface brightness relation seen in their data. The global surface brightness distribution may indeed be flat but the low surface brightness systems are predominantly dwarfs, providing little enhancement to the global luminosity, baryon or mass densities. We have attempted to address this debate through careful consideration of *most* selection issues. We probe to depths where the distribution is clearly bounded and where we robustly demonstrate we could reliably recover giant low surface brightness galaxies were they to exist in significant numbers. They do not.

While we address the selection bias in the redshift survey as a function of apparent magnitude and apparent surface brightness other potential selection effects remain unexplored. For example, the redshift completeness may well be a function of spectral type, in which case the assumption that all galaxies of similar apparent magnitude and surface brightness are drawn from the same redshift distribution will not be correct. In particular, inert low surface brightness galaxies which may have insufficient features to readily yield a redshift and may be missed entirely. We also do not at this stage decompose galaxies into bulge and disk components. This is clearly required by both the observations (which show two, or possibly three, distinct luminosity-surface brightness relations for spheroid and disk components) as well as by theory and simulations which argue for distinct formation mechanisms for these components (merger and accretion respectively; e.g. Pierani, Mohayaee & de Freitas Pacheco 2004). We hence intend to extend our analysis in three ways: 100 per cent spectroscopic completeness; bulge-disk decompositions; and extension to longer wavelengths and in particular the near-IR which promises smoother, dust-free profiles.

### ACKNOWLEDGMENTS

We thank Shiyin Shen, Eric Bell and Michael Blanton for useful discussions and exchange of data, Steve Phillipps, Alister Graham and Stefan Andreon for comments on the early drafts and the referee for a number of detailed scientific and stylistic improvements.

The Millennium Galaxy Catalogue consists of imaging data from the Isaac Newton Telescope and spectroscopic data from the Anglo Australian Telescope, the ANU 2.3m, the ESO New Technology Telescope, the Telescopio Nazionale Galileo, and the Gemini Telescope. The survey has been supported through grants from the Particle Physics and Astronomy Research Council (UK) and the Australian Research Council (AUS). The data and data products are publicly available from <http://www.eso.org/~jliske/mgc/> or on request from J. Liske or S.P. Driver.

This research has made use of the NASA/IPAC Extragalactic Database (NED) which is operated by the Jet Propulsion Laboratory, California Institute of Technology, under contract with the National Aeronautics and Space Administration.

This research made use of mock catalogues constructed by the Durham astrophysics group and the VIRGO consortium.

Funding for the Sloan Digital Sky Survey (SDSS) has been provided by the Alfred P. Sloan Foundation, the Participating Institutions, the National Aeronautics and Space Administration, the National Science Foundation, the U.S. Department of Energy, the Japanese Monbukagakusho, and the Max Planck Society. The SDSS Web site is <http://www.sdss.org/>. The SDSS is managed by the Astrophysical Research Consortium (ARC) for the Participating Institutions. The Participating Institutions are The University of Chicago, Fermilab, the Institute for Advanced Study, the Japan Participation Group, The Johns Hopkins University, Los Alamos National Laboratory, the Max-Planck-Institute for Astronomy (MPIA), the Max-Planck-Institute for Astrophysics (MPA), New Mexico State University, University of Pittsburgh, Princeton University, the United States Naval Observatory, and the University of Washington.

## REFERENCES

- Abazajian K. et al., 2003, *AJ*, 126, 2081  
 Andreon S., Cullandire, J.-C., 2002, *ApJ*, 569, 144  
 Baldry I., Glazebrook K., Brinkmann J., Ivezić Z., Lupton R.H., Nichol R.C., Szalay A.S., 2004, *ApJ*, 600, 681  
 Bell E., Baugh C.M., Cole S., Frank C.S., Lacey C.G., 2003, *MNRAS*, 343, 367  
 Bernardi M. et al., 2003, *AJ*, 125, 1849  
 Bertin E., Arnouts S., 1996, *A&AS*, 117, 393  
 Binggeli B., Sandage A., Tammann G.A., 1988, *ARA&A*, 26, 509  
 Blanton M.R. et al., 2001, *AJ*, 121, 2358  
 Blanton M.R. et al., 2003a, *ApJ*, 592, 819  
 Blanton M.R. et al., 2003b, *ApJ*, 594, 186  
 Blanton M.R., Lupton R.H., Schlegel D.J., Strauss M.A., Brinkmann J., Fukugita M., Loveday J., 2005a, *ApJ*, submitted, (astro-ph/0410164)  
 Blanton M., et al., 2005b, *AJ*, submitted, (astro-ph/0410166)  
 Boyce P., Phillipps S., 1995, *A&A*, 296, 26  
 Buchalter A., Jimenez R., Kamionkowski M., 2001, *MNRAS*, 328, 520  
 Bullock J., Dekel A., Kolatt T.S., Kravtsov A.V., Klypin A.A., Porciani C., Primack J.R., 2001, *ApJ*, 555, 240  
 Chen H.-W., Lanzetta K., 2003, *ApJ*, 597, 706  
 Murali C., Katz N., Hernquist L., Weinberg D., Romeel D., 2002, *ApJ*, 571, 1  
 Chofoniewski J., 1985, *MNRAS*, 214, 197  
 Cole S., Lacey C., 1996, *MNRAS*, 281, 716  
 Cole S., Hattón S., Weinberg D.H., Frenk C.S., 1998, *MNRAS*, 300, 945  
 Colless M. et al., 2001, *MNRAS*, 328, 1039  
 Croom S.M., Smith R.J., Boyle B.J., Shanks T., Loaring N.S., Miller L., Lewis I.J., 2001, *MNRAS*, 322, 29  
 Cross N.J.G. et al., 2001, *MNRAS*, 324, 825  
 Cross N.J.G., Driver S.P., 2002, *MNRAS*, 329, 579  
 Cross N.J.G., Driver S.P., Liske J., Lemon D.J., Peacock J.A., Cole S., Norberg P., Sutherland W.J., 2004, *MNRAS*, 349, 576  
 Dalcanton J.J., 1998, *ApJ*, 495, 251  
 Dalcanton J.J., Spergel D., Summers F.J., 1997, *ApJ*, 482, 659  
 Davis M., Huchra J., 1982, *ApJ*, 254, 437  
 de Lapparent V., 2003, *A&A*, 408, 845  
 de Jong R.S., Lacey C., 2000, *ApJ*, 545, 781  
 de Jong R.S., Simard L., Davies R.L., Saglia R.P., Burstein D., Colless M., McMahan R., Wegner G., 2004, *MNRAS*, 355, 1155  
 De Propris R., Liske J., Driver S.P., Allen P.D., Cross N.J.G., 2005, submitted  
 Disney M.J., 1976, *Nature*, 263, 573  
 Disney M.J., Davies J.I., Phillipps S., 1989, *MNRAS*, 239, 939  
 Driver S.P., 1999, *ApJ*, 526, 69  
 Driver S.P., 2004, *PASA*, 21, 344  
 Driver S.P., De Propris R., 2003, *Ap&SS*, 285, 175  
 Driver S.P., Couch W.J., Phillipps S., 1998, *MNRAS*, 301, 369  
 Driver S.P., Phillipps S., Morgan I., Davies J.I., Disney M.J., 1994, *MNRAS*, 268, 393  
 Efstathiou G., Ellis R.S., Peterson B.A., 1988, *MNRAS*, 232, 431  
 Fall M., Efstathiou G., 1980, *MNRAS*, 193, 189  
 Ferguson H.C., Binggeli B., 1994, *A&ARv*, 6, 67  
 Francis P.J., Nelson B.O., Cutri R.M., 2004, *AJ*, 127, 646  
 Freeman K.C., 1970, *AJ*, 160, 811  
 Graham A., Guzman R., 2003, *AJ*, 125, 2936  
 Impey C., Bothun G.D., Malin D., 1988, *ApJ*, 330, 634  
 Impey C., Bothun G.D., 1997, *ARA&A*, 35, 267  
 Impey C.D., Sprayberry D., Irwin M.J., Bothun G.D., 1996, *AJ*, 112, 865  
 Karachentsev I.D. et al., 2002, *A&A*, 389, 812  
 Karachentsev, I.D., Karachentseva V.E., Huchtmeier W.K., Makarov D.I., 2004, *AJ*, 127, 2031  
 Kennicutt R., 1989, *ApJ*, 498, 541  
 Kormendy J., 1977, *ApJ*, 218, 333  
 Lemon D., Wyse R.F.G., Liske J., Driver S.P., Horne K., 2004, *MNRAS*, 347, 1043  
 Liske J., Lemon D., Driver S.P., Cross N.J.G., Couch W.J., 2003, *MNRAS*, 344, 307  
 Marzke R.O., da Costa L.N., Pellegrini P.S., Willmer C.N.A., Geller M.J., 1998, *ApJ*, 503, 617  
 Mateo M., 1998, *ARA&A*, 36, 435  
 Mo S., Mao H.J., White S.D.M., 1998, *MNRAS*, 297, 71  
 Nakamura O., Fukugita M., Yasuda N., Loveday J., Brinkmann J., Schneider D.P., Shimasaku K., SubbaRao, M., 2003, *ApJ*, 125, 1682  
 Norberg P. et al., 2002, *MNRAS*, 336, 907  
 O'Neil K., Andreon A., Cullandire J.-C., 2003, *A&A*, 399, 35  
 Patton D.R., Carlberg R.G., Marzke R.O., Pritchett C.J., da Costa L.N., Pellegrini P.S., 2000, *ApJ*, 536, 153  
 Peacock J.A. et al., 2001, *Nature*, 410, 169  
 Peebles J., 1969, *ApJ*, 155, 393  
 Pierani S., Mohayaee R., de Freitas Pacheco J.A., 2004, *MNRAS*, 348, 921  
 Phillipps S., Driver S.P., 1995, *MNRAS*, 274, 832  
 Phillipps S., Davies J.I., Disney M.J., 1990, *MNRAS*, 242, 235  
 Poggianti B., 1997, *A&AS*, 122, 399  
 Popesso P., Boehringer H., Romaniello M., Voges W., 2004, *A&A*, in press, (astro-ph/0410011)  
 Press W.H., Teukolsky S.A., Vetterlin W.T., Flannery B.P., 1992, in *Numerical Recipes*, (Publ: Cambridge)  
 Roberts S., Davies J.I., Sabatini S., van Driel W., O'Neil K., Baes M., Linder S., Smith R., Evans R., 2004, *MNRAS*, 352, 478  
 Schechter P., 1976, *ApJ*, 203, 297  
 Shen S., Mo H.J., White S.D.M., Blanton M.R., Kauffmann G., Voges W., Brinkmann J., Csabai I., 2003, *MNRAS*, 343, 978  
 Silk J., Rees M., 1998, *A&A*, 331, 1  
 Simard L. et al., 2002, *ApJS*, 142, 1  
 Sodr e L., Jr., Lahav O., 1993, *MNRAS*, 260, 285

- Sprayberry D., Impey C., Irwin M.J., Bothun G.D., 1997, ApJ, 482, 104  
Trentham N., 1998, MNRAS, 293, 71  
Vitvitska M., Klypin A.A., Kravtsov A.V., Wechsler R.H., Primack J.R., Bullock J.S., 2002, ApJ, 581, 799  
Zucca E. et al., 1997, A&A, 326, 477  
Zwaan M., Briggs F.H., Sprayberry D., Sorar E., 1997, ApJ, 490, 173  
Zwicky F., 1957, in *Morphological Astronomy* (Publ: Princeton)

**Table 1.** The breakdown of the survey contributions to the final MGC redshift sample.

Survey	No. of galaxies with $Q_z \geq 3$	No. of best redshifts	Reference
MGCz	5054	4944	This work
SDSS-DR1	2909	1528	Abazajian et al. (2003)
2dFGRS	4129	3152	Colless et al. (2001)
2QZ	19	13	Croom et al. (2001)
PF	37	28	Francis et al. (2004)
LSBG	11	2	Impey et al. (1996)
NED	1200	29	NED

**Table 2.** Choloniewski (upper) and Schechter (lower) function parameters for the MGC galaxy distribution and comparable parameters from other surveys corrected to the  $B_{\text{MGC}}$  bandpass. MGC BBD refers to the empirical MGC BBD integrated over surface brightness. Values are for  $\Omega_M = 0.3$ ,  $\Omega_\Lambda = 0.7$  and  $H_0 = 100 \text{ km s}^{-1}$ .

Survey	Filter	$\phi^*$ $10^{-2} h^3 \text{ Mpc}^{-3}$	$M_{B_{\text{MGC}}}^*$ mag	$\alpha$	$\mu^{e*}$ mag arcsec $^{-2}$	$\beta$	$\sigma_{\mu^e}$ mag arcsec $^{-2}$	Ref
MGC (All types)	$B_{\text{MGC}}$	$2.13 \pm 0.32$	$-19.37 \pm 0.15$	$-0.99 \pm 0.14$	$22.0 \pm 0.13$	$0.33 \pm 0.15$	$0.86 \pm 0.09$	1
Spheriods	$B$	—	$-19.70^a$	—	20.03	-1.57	0.38	2
Disks	$B$	—	$-19.70^a$	—	22.77	0.0	0.3	3
HDF (All types)	$B_{AB} + 0.13$	—	$-19.70^a$	—	$20.9 \pm 0.8$	$0.67 \pm 0.09$	1	4
E/S0s (Total)	$R + 1.4$	$0.010 \pm 0.002$	$-20.7 \pm 0.2$	$1.06 \pm 0.26$	$20.8 \pm 0.4$	$0.92 \pm 0.09$	$-0.62 \pm 0.08$	5
E/S0s (Bulges)	$R + 1.4$	$0.008 \pm 0.003$	$-20.1 \pm 0.3$	$1.30 \pm 0.50$	$20.32 \pm 0.35$	$0.84 \pm 0.09$	$-0.55 \pm 0.10$	5
Sd/Irrs(Total)	$I_C + 1.8$	$0.332 \pm 0.07$	$-19.7 \pm 0.1$	$-0.93 \pm 0.10$	$21.8 \pm 0.2$	$0.51 \pm 0.04$	$0.61 \pm 0.04$	6
Sd/Irrs(Disk)	$I_C + 1.8$	$0.332 \pm 0.07$	$-19.9 \pm 0.1$	$-0.90 \pm 0.10$	$21.7 \pm 0.2$	$0.43 \pm 0.05$	$0.78 \pm 0.07$	6
2dFGRS	$b_{2dF} + 0.06$	$2.06 \pm 0.09$	$-19.67 \pm 0.02$	$-1.05 \pm 0.04$	$21.90 \pm 0.02$	$0.28 \pm 0.02$	$0.57 \pm 0.01$	7
SDSS(Early)	$r_{0.1} + 1.3$	—	$-19.70^a$	—	19.4	1.2	$0.6 - 1.2$	8
SDSS(Late)	$r_{0.1} + 0.9$	—	$-19.70^a$	—	21.35	0.54	$0.6 - 1.0$	8
MGC BBD	$B_{\text{MGC}}$	$1.77 \pm 0.15$	$-19.60 \pm 0.04$	$-1.13 \pm 0.02$	—	—	—	1
ESP	$b_j + 0.13$	$1.65 \pm 0.3$	$-19.59 \pm 0.08$	$-1.22 \pm 0.07$	—	—	—	9
SDSS1	$g + 0.40$	$2.06 \pm 0.23$	$-19.64 \pm 0.04$	$-1.26 \pm 0.05$	—	—	—	10
2dFGRS	$b_{2dF} + 0.06$	$1.61 \pm 0.06$	$-19.60 \pm 0.008$	$-1.21 \pm 0.01$	—	—	—	11
SDSS2 <sub>0.0</sub>	$^{0.1}g - 0.09$	$2.12 \pm 0.08$	$-19.28 \pm 0.02$	$-0.89 \pm 0.03$	—	—	—	12
SDSS2 <sub>0.1</sub>	$^{0.1}g - 0.09$	$2.18 \pm 0.08$	$-19.48 \pm 0.02$	$-0.89 \pm 0.03$	—	—	—	12

<sup>a</sup> Adopted value.

References: (1) This work. (2) Kormendy (1977). (3) Freeman (1970). (4) Driver (1999). (5) de Jong et al. (2004). (6) de Jong &amp; Lacey (2000). (7) Cross et al. (2001). (8) Shen et al. (2003). (9) Zucca et al. (1997). (10) Blanton et al. (2001). (11) Norberg et al. (2002). (12) Blanton et al. (2003a) with and without evolution corrections.

**Table 3.** Gaussian fits to the surface brightness distribution in various intervals of absolute magnitude. Surface brightness is defined as the mean surface brightness within the half-light semi-major axis (i.e., using elliptical apertures).

$M_{B_{\text{MGC}}} - 5 \log h$ mag	$\mu^{e*}$ mag arcsec $^{-2}$	$\sigma_{\mu^e}$ mag arcsec $^{-2}$	$\phi^*$ $10^{-3} h^3 \text{ Mpc}^{-3}$	$\chi^2/\nu$
-21.25	$21.86 \pm 0.10$	$0.48 \pm 0.12$	$0.08 \pm 0.02$	4.0/5
-20.75	$21.72 \pm 0.04$	$0.58 \pm 0.03$	$0.34 \pm 0.03$	14.0/10
-20.25	$21.86 \pm 0.02$	$0.74 \pm 0.01$	$1.37 \pm 0.06$	5.67/10
-19.75	$21.86 \pm 0.01$	$0.74 \pm 0.01$	$2.64 \pm 0.09$	10.5/9
-19.25	$21.94 \pm 0.01$	$0.80 \pm 0.01$	$4.33 \pm 0.10$	16.4/10
-18.75	$22.10 \pm 0.02$	$0.90 \pm 0.01$	$5.96 \pm 0.13$	30.5/11
-18.25	$22.32 \pm 0.03$	$1.00 \pm 0.01$	$7.29 \pm 0.22$	27.6/9
-17.75	$22.58 \pm 0.03$	$1.06 \pm 0.02$	$8.86 \pm 0.27$	7.61/9
-17.25	$22.86 \pm 0.07$	$1.22 \pm 0.07$	$9.69 \pm 0.65$	16.6/9
-16.75	$23.00 \pm 0.09$	$1.06 \pm 0.07$	$9.48 \pm 0.68$	22.7/8
-16.25	$23.16 \pm 0.12$	$1.20 \pm 0.10$	$13.9 \pm 0.9$	16.0/7
-15.75	$23.42 \pm 0.11$	$0.86 \pm 0.12$	$11.5 \pm 2.1$	4.12/7
-15.25	$23.34 \pm 0.24$	$1.32 \pm 0.20$	$17.9 \pm 3.0$	6.85/7
-14.75	$24.26 \pm 0.43$	$1.50 \pm 0.16$	$19.8 \pm 3.7$	4.31/6
-14.25	$23.28 \pm 0.64$	$1.14 \pm 0.40$	$23.0 \pm 7.9$	1.38/3

## APPENDIX A: SIMULATIONS

Galaxy sampling, detection and analysis selection effects are extremely complex (see e.g. Disney, Davies & Phillipps 1989) and depend on: galaxy profile; inclination; opacity; detector characteristics; survey depth and resolution; and the detection and analysis process, in particular background smoothing and removal. In this appendix we intend to crudely establish the empirical selection limits of the MGC through simulations. The equations defining the redshift dependent selection limits are described in Section 3.5 (see also Driver 1999) and require a maximum and minimum size limit and a limiting surface brightness. In addition, we need a method to correct the observed half-light radii of compact galaxies for the effects of seeing.

To establish the selection limits and the correction procedure we use IRAF’s ARTDATA package to simulate  $45^\circ$ -inclined optically thin exponential disks (this is consistent with our definition of surface brightness, see Section 3.4) on a CCD frame with identical pixel size, sky noise and seeing as the MGC imaging data (i.e.,  $0.333 \text{ arcsec/pixel}$ ,  $\mu_{\text{LM}} = 26 \text{ mag arcsec}^{-2}$  and  $\Gamma = 1.27 \text{ arcsec}$ ). We produce simulation plates at 0.5 mag intervals from  $m_{\text{in}} = 16$  to 20 mag, each containing galaxies with half-light radii varying from  $r_{\text{in}} = 0.1$  to 32 arcsec (see Fig. A1). Compact galaxies were also simulated with de Vaucouleurs profiles but the results were the same as those for exponential disks.

The MGC catalogue was derived using the SExtractor analysis software (Bertin & Arnouts 1996). The full details of this process are described in Liske et al. (2003). We use SExtractor in an identical manner (e.g., sky background mesh  $256 \times 256$  pixels with  $7 \times 7$  filtering within each mesh) on the simulated data and also measure half-light radii in the same way as for the real data.

Tables A1-A3 contain the results of our simulations as a function of  $m_{\text{in}}$  and  $r_{\text{in}}$  and these are also presented in Fig. A2.

### A1 Seeing correction

From the top left panel of Fig. A2 we can see the impact of the seeing, which was set to the median value of our survey. To crudely correct for this effect we make the reasonable assumption that the observed half-light radius,  $r_e$ , is given by the quadratic sum of the true half-light radius,  $r_e^0$ , and some fraction,  $\eta$ , of the seeing FWHM,  $\Gamma$ :

$$r_e^2 = (r_e^0)^2 + \eta \Gamma^2. \quad (\text{A1})$$

From the real MGC data we find that the median  $r_e$  of stars is well described by  $0.6 \Gamma$  (for a perfectly Gaussian PSF this would be  $0.5 \Gamma$ ) and hence one would expect  $\eta = 0.36$ . However, from the simulations we find  $\eta = 0.32$  and that equation (A1) recovers the true half-light radii to an accuracy of better than 10 per cent for objects not classified as stars (see top right panel of Fig. A2).

### A2 Minimum size limit

The most compact simulated galaxies are routinely classified as stars by the SExtractor star-galaxy separation and these objects are marked with an asterisk in Table A1. SExtractor’s ability to distinguish a galaxy of given  $r_e$  from stars cannot primarily depend on the absolute value of  $r_e$ . It must rather depend on the galaxy’s distance,  $\Delta$ , from the stellar locus in  $r_e$ -space, where the scale of that distance is set by the width of the stellar  $r_e$  distribution. From the MGC data we find the width of that distribution to be independent of seeing. Hence the minimum  $\Delta$  at which a galaxy can still be reliably distinguished from stars cannot depend on seeing either. Recalling that the position of the stellar locus is given by  $0.6 \Gamma$  we thus find:

$$r_{\text{MIN}} = 0.6 \Gamma + \Delta_{\text{MIN}} \quad (\text{A2})$$

**Table A1.** The recovered half-light radii ( $r_{\text{out}}$ , uncorrected for seeing) from our simulations. Objects marked with a \* were classified as stars by SExtractor.

$r_{\text{in}}$ arcsec	Simulated magnitude ( $m_{\text{in}}$ )								
	16.0	16.5	17.0	17.5	18.0	18.5	19.0	19.5	20.0
0.1	0.63*	0.63*	0.63*	0.64*	0.64*	0.64*	0.67*	0.66*	0.68*
0.2	0.67*	0.67*	0.67*	0.67*	0.67*	0.67*	0.67*	0.68*	0.70*
0.4	0.77*	0.77*	0.77*	0.78*	0.77*	0.78*	0.78*	0.77*	0.78*
0.8	1.07*	1.07*	1.07	1.07	1.07	1.07	1.07	1.07	1.07
1.0	1.27*	1.27*	1.25	1.25	1.27	1.25	1.22	1.20	1.20
1.2	1.40	1.40	1.40	1.40	1.40	1.40	1.38	1.38	1.38
1.5	1.67	1.67	1.67	1.67	1.67	1.67	1.67	1.67	1.65
2	2.13	2.13	2.13	2.13	2.08	2.11	2.08	2.13	2.16
4	4.00	4.00	4.00	4.00	4.00	4.00	3.89	4.00	4.00
6	5.55	5.66	5.66	5.88	5.77	5.77	5.77	5.66	5.44
8	7.99	7.66	8.10	7.99	7.88	7.77	7.44	6.88	
10	9.66	9.66	9.99	10.21	9.77	9.54	8.66		
12	11.32	11.32	12.10	12.21	11.43	10.99			
15	13.65	13.99	14.77	15.21	14.32	12.54			
20	18.32	17.98	21.32	18.87	15.65				
22	19.87	19.42	22.98	20.42					
24	20.42	20.98	25.31	21.43					
26	21.42	22.53	26.86	22.76					
28	23.09	23.53	28.97	24.42					
30	23.64	24.64	30.30						
32	24.09	25.20	31.75						

To determine  $\Delta_{\text{MIN}}$  we note from Table A1 that in the simulations the confusion between stars and galaxies sets in at  $r_{\text{MIN}}(\Gamma = 1.27) = 1.07$  arcsec, implying  $\Delta_{\text{MIN}} = 0.31$  arcsec. The same value is found by fitting the actually observed minimum  $r_e$  of galaxies in each MGC field as a function of  $\Gamma$ .

Finally, combining equations (A1) and (A2) we find the minimum seeing-corrected half-light radius:

$$r_{\text{MIN}}^0 = \sqrt{0.04 \Gamma^2 + 0.37 \Gamma + 0.1} \quad (\text{A3})$$

### A3 Maximum size and low surface brightness limits

Here we define these limits (on the seeing-corrected quantities) not as absolute detection limits but rather as the limits to which we can expect ‘reliable’ photometry. We arbitrarily define ‘reliable’ to mean magnitude and surface brightness estimates accurate to 0.1 mag and 0.1 mag arcsec<sup>-2</sup> respectively, thereby limiting the potential systematics due to isophotal errors and background subtraction to 0.1 mag and 0.1 mag arcsec<sup>-2</sup>. As most of our analysis uses 0.5 mag and 0.5 mag arcsec<sup>-2</sup>-sized bins this ensures minimal impact of systematics on our final BBD.

To determine  $r_{\text{MAX}}^0$  and  $\mu_{\text{LIM}}^0$  we proceed in the following way: using Tables A2 and A3 we find for a given  $m_{\text{in}}$  the smallest  $r_{\text{in}}$  for which either the recovered magnitude,  $m_{\text{out}}$ , or the recovered (seeing-corrected) surface brightness  $\mu_{\text{out}}^0$  differs by at least 0.1 mag or 0.1 mag arcsec<sup>-2</sup> from the respective input value. Given the resulting pair of  $(m_{\text{in}}, r_{\text{in}})$  values we again use Tables A2 and A3 to find the corresponding  $(m_{\text{out}}, \mu_{\text{out}}^0)$  pair and plot this on Fig. 9 (lower square points with errorbars). Finally, we find those values of  $r_e^0$  and surface brightness which best fit these points. We find

$$r_{\text{MAX}}^0 = 15 \text{ arcsec} \quad (\text{A4})$$

and

$$\mu_{\text{LIM}}^0 = 25.25 \text{ mag arcsec}^{-2}. \quad (\text{A5})$$

Finally it is worth noting that some of the extreme low surface brightness galaxies were detected by SExtractor but they were broken up into numerous small objects. Rerunning SExtractor over the entire MGC with the deblender switched off may enable us to eventually probe fainter than the limits determined here, however a detailed study of the MGC using a cross-correlation method (Roberts et al. 2004) failed to find any additional galaxies.



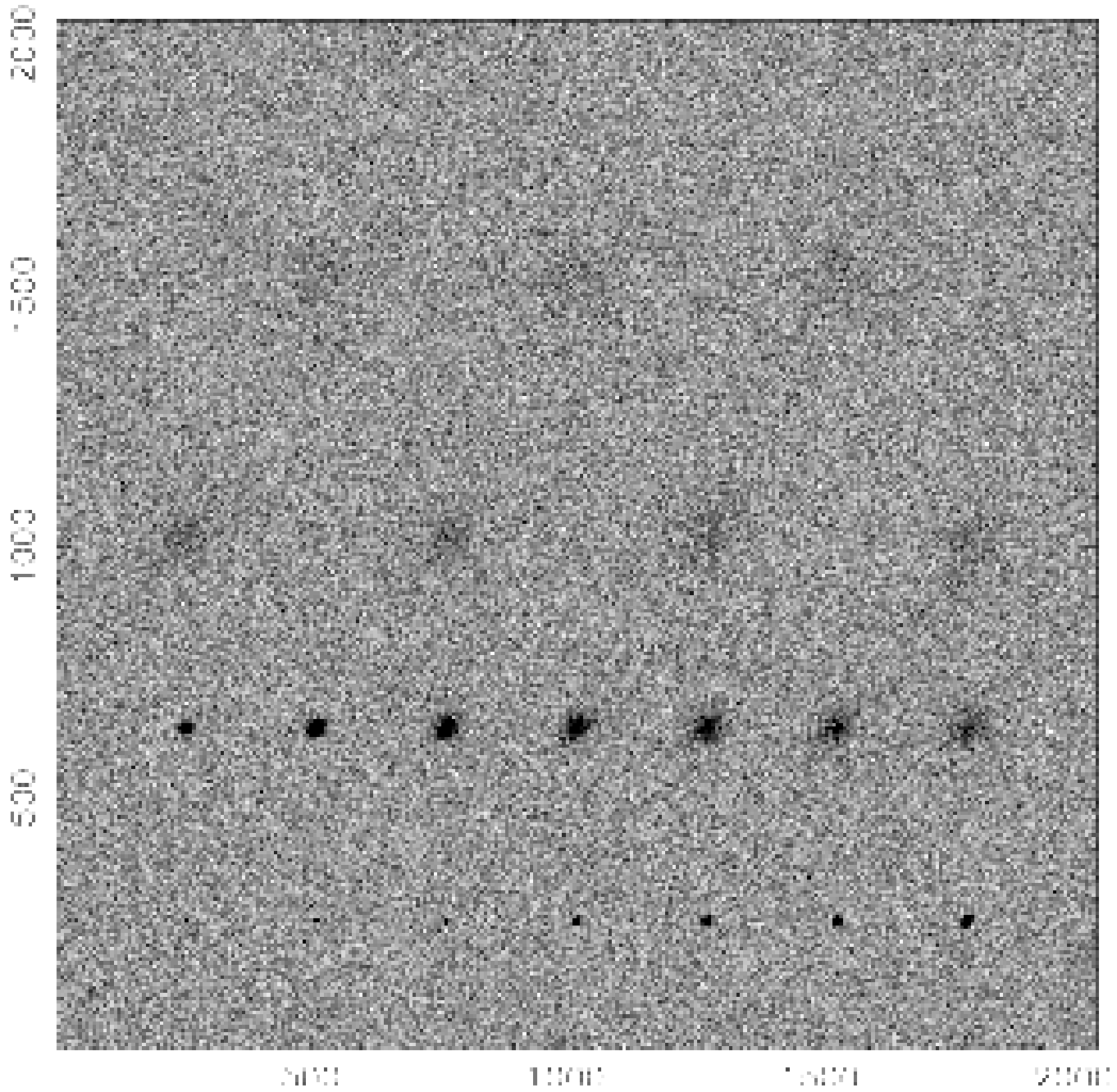


**Figure A1.** A simulated image showing  $45^\circ$ -inclined exponential profile galaxies all with magnitude 18 mag, but with half-light radii varying from 0.1 to 32 arcsec (from left-to-right and bottom-to-top 0.1, 0.2, 0.4, 0.8, 1.0, 1.2, 1.5, 2, 4, 6, 8, 10, 12, 15, 20, 22, 24, 26, 28, 30, 32 arcsec). X and Y units are in pixels ( $\equiv 0.333$  arcsec). Figure degraded see <http://www.eso.org/~jlliske/mgc/> for full pdf copy of this paper.

**Table A2.** The recovered magnitudes ( $m_{\text{out}}$ ) from our simulations.

$r_{\text{in}}$ arcsec	Simulated magnitude ( $m_{\text{in}}$ )								
	16.0	16.5	17.0	17.5	18.0	18.5	19.0	19.5	20.0
0.1	16.00	16.50	17.00	17.50	18.00	18.50	19.00	19.50	20.00
0.2	16.00	16.50	17.00	17.50	18.00	18.33	19.00	19.50	20.00
0.4	16.00	16.50	17.00	17.50	18.00	18.49	19.00	19.52	19.99
0.8	16.01	16.51	17.01	17.51	18.01	18.50	19.01	19.51	20.02
1.0	16.01	16.51	17.01	17.51	18.01	18.51	19.01	19.53	20.01
1.2	16.01	16.51	17.01	17.51	18.01	18.52	19.03	19.53	20.02
1.5	16.02	16.52	17.02	17.52	18.02	18.52	19.02	19.51	20.00
2	16.02	16.52	17.02	17.52	18.02	18.52	19.03	19.54	20.03
4	16.03	16.53	17.02	17.53	18.03	18.55	19.08	19.58	20.10
6	16.03	16.54	17.03	17.52	18.03	18.55	19.09	19.64	20.23
8	16.05	16.56	17.02	17.50	18.04	18.58	19.13	19.73	
10	16.06	16.57	17.00	17.47	18.02	18.55	19.16		
12	16.09	16.58	17.00	17.46	18.03	18.61			
15	16.14	16.59	17.03	17.44	18.30	18.68			
20	16.11	16.63	16.89	17.48	18.17				
22	16.13	16.65	16.88	17.49	12.13				
24	16.23	16.67	16.89	17.57					
26	16.26	16.70	16.81	17.51					
28	16.27	16.72	16.91	17.66					
30	16.34	16.79	16.80						
32	16.40	16.78	16.82						

**Table A3.** The input ( $\mu_{\text{in}}$ , left) and seeing-corrected output ( $\mu_{\text{out}}^0$ , right) effective surface brightnesses from our simulations. Objects classified as stars are indicated by \*\*\*\*\* and objects not detected are indicated by —.

$r_{\text{in}}$ arcsec	Simulated magnitude ( $m_{\text{in}}$ )									
	16.0	16.5	17.0	17.5	18.0	18.5	19.0	19.5	20.0	
0.1	13.00 *****	13.50 *****	14.00 *****	14.50 *****	15.00 *****	15.50 *****	16.00 *****	16.50 *****	17.00 *****	17.00 *****
0.2	14.50 *****	15.00 *****	15.50 *****	16.00 *****	16.50 *****	17.00 *****	17.50 *****	18.00 *****	18.50 *****	18.50 *****
0.4	16.01 *****	16.51 *****	17.01 *****	17.51 *****	18.01 *****	18.51 *****	19.01 *****	19.51 *****	20.01 *****	20.01 *****
0.8	17.51 *****	18.01 *****	18.51 18.50	19.01 19.00	19.51 19.50	20.01 19.99	20.51 20.50	21.01 21.00	21.51 21.51	21.51 21.51
1.0	18.00 *****	18.50 *****	19.00 19.06	19.50 19.56	20.00 20.11	20.50 20.56	21.00 20.98	21.50 21.44	22.00 21.92	22.00 21.92
1.2	18.39 18.40	18.89 18.90	19.39 19.40	19.89 19.90	20.39 20.40	20.89 20.91	21.39 21.38	21.89 21.88	22.39 22.37	22.39 22.37
1.5	18.88 18.91	19.38 19.41	19.88 19.91	20.38 20.41	20.88 20.91	21.38 21.41	21.88 21.91	22.38 22.40	22.88 22.85	22.88 22.85
2	19.50 19.53	20.00 20.03	20.50 20.53	21.00 21.03	21.50 21.47	22.00 22.00	22.50 22.48	23.00 23.05	23.50 23.57	23.50 23.57
4	21.01 21.00	21.51 21.50	22.01 21.99	22.51 22.50	23.01 23.00	23.51 23.52	24.01 23.99	24.51 24.55	25.01 25.07	25.01 25.07
6	21.89 21.73	22.39 22.28	22.89 22.77	23.39 23.35	23.89 23.81	24.39 24.33	24.89 24.87	25.39 25.38	25.89 25.88	25.89 25.88
8	22.51 22.55	23.01 22.97	23.51 23.55	24.01 24.00	24.51 24.51	25.01 25.02	25.51 25.47	26.01 25.90	26.51 —	26.51 —
10	23.00 22.97	23.50 23.48	24.00 23.99	24.50 24.51	25.00 24.96	25.50 25.44	26.00 25.84	26.50 —	27.00 —	27.00 —
12	23.39 23.35	23.89 23.84	24.39 24.41	24.89 24.89	25.39 25.31	25.89 25.81	26.39 —	26.89 —	27.39 —	27.39 —
15	23.88 23.81	24.38 24.31	24.88 24.87	25.38 25.34	25.88 26.07	26.38 26.16	26.88 —	27.38 —	27.88 —	27.88 —
20	24.50 24.42	25.00 24.90	25.50 25.53	26.00 25.85	26.50 26.14	27.00 —	27.50 —	28.00 —	28.50 —	28.50 —
22	24.71 24.61	25.21 25.09	25.71 25.68	26.21 26.03	26.71 —	27.21 —	27.71 —	28.21 —	28.71 —	28.71 —
24	24.90 24.77	25.40 25.27	25.90 25.90	26.40 26.22	26.90 —	27.40 —	27.90 —	28.40 —	28.90 —	28.90 —
26	25.07 24.91	25.57 25.46	26.07 25.95	26.57 26.29	27.07 —	27.57 —	28.07 —	28.57 —	29.07 —	29.07 —
28	25.23 25.08	25.73 25.57	26.23 26.21	26.73 26.59	27.23 —	27.73 —	28.23 —	28.73 —	29.23 —	29.23 —
30	25.38 25.20	25.88 25.74	26.38 26.20	26.88 —	27.38 —	27.88 —	28.38 —	28.88 —	29.38 —	29.38 —
32	25.52 25.30	26.02 25.78	26.52 26.32	27.02 —	27.52 —	28.02 —	28.52 —	29.02 —	29.52 —	29.52 —

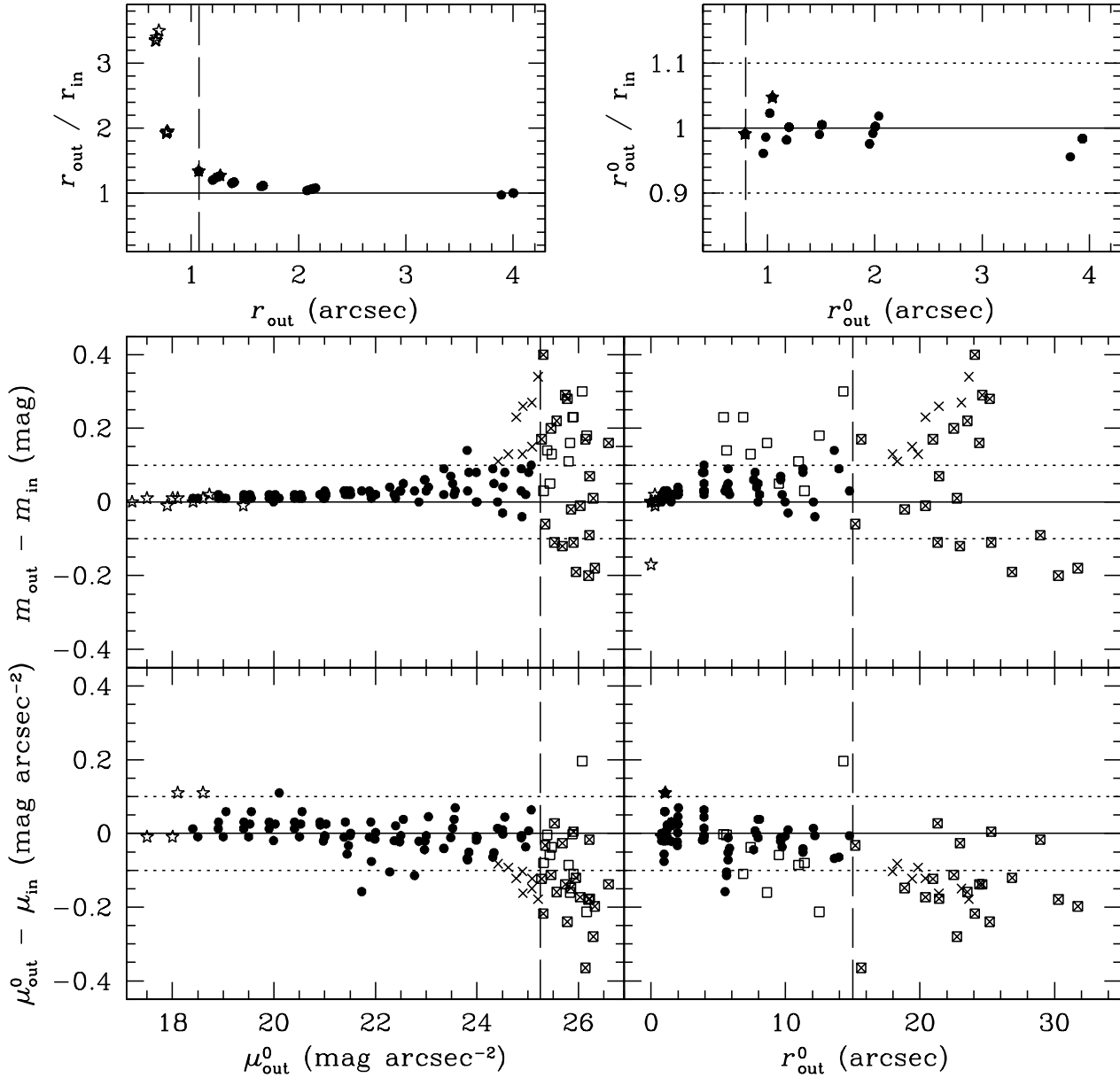


**Figure A2.** A graphical representation of Tables A1, A2 and A3. The top panels show the ratio of the output and input half-light radii both with (right) and without (left) seeing correction. These panels demonstrate the effectiveness of the seeing correction. The dashed lines show the minimum size limit  $r_{\text{MIN}} = 0.6\Gamma + 0.31$  arcsec. The middle panels show the difference between the output and input magnitudes as a function of the seeing-corrected output half-light radius ( $r_{\text{out}}^0$ , right) and as a function of the seeing-corrected output effective surface brightness ( $\mu_{\text{out}}^0$ , left). Finally, the bottom panels show difference between the seeing-corrected output and input surface brightnesses as a function of the same two parameters. The dashed lines in the left panels show the low surface brightness limit  $\mu_{\text{LIM}}^0 = 25.25$  mag arcsec $^{-2}$ , while in the right panels they mark the maximum size limit  $r_{\text{MAX}}^0 = 15$  arcsec. In all panels we show objects identified as stars by SExtractor as open star symbols, objects beyond  $r_{\text{MAX}}^0$  as crosses and objects beyond  $\mu_{\text{LIM}}^0$  as open squares. Solid symbols represent galaxies within the selection limits and for these we recover magnitudes and surface brightnesses that lie consistently within  $\pm 0.1$  mag and  $\pm 0.1$  mag arcsec $^{-2}$  of their input values.